Asia-Pacific Journal of Atmospheric Sciences (2025) 61:27
https://doi.org/10.1007/s13143-025-00410-x

Online ISSN 1976-7951
Print ISSN 1976-7633

ORIGINAL ARTICLE

Improvement of Dust Retrieval Algorithm Using GK-2 A Geo Satellite Thermal Infrared Channels by Establishing Observation-based Refractive Index Dataset Tailored for East Asian Dust

Ehsan Parsa Javid[1] · Sang Seo Park[1,2] · Hyunkwang Lim[3] · Kwang-Mog Lee[4]

Received: 17 March 2025 / Revised: 25 July 2025 / Accepted: 12 August 2025 / Published online: 10 October 2025

Abstract

Applying assumptions about the optical properties of dust, particularly the refractive index (RI), introduces significant uncertainty in thermal infrared dust-retrieval algorithms. To address this, we present a tailored RI dataset (ERML 2025) for Asian dust, derived from long-term chemical composition measurements in South Korea. An enhanced algorithm was developed using this Asian dust RI and thermal infrared channels from the GK-2 A Korean geostationary satellite. This LUT-based algorithm integrates three methods for dust layer height estimation: the Unified Model (UM), the Asian Dust Aerosol Model 3 (ADAM3), and a fixed-height approach. Operational dust detection processes and consistent assumptions were applied to minimize confounding variables in sensitivity tests. Qualitative validation using GK-2 A RGB and IASI-LMD products showed strong alignment in some regions and notable mismatches elsewhere, likely due to dust detection performance. Quantitative comparisons were conducted using MODIS data. Sensitivity analyses demonstrated that the combined use of the updated algorithm and UM model improved the operational method in most cases. Results also indicated that the updated algorithm retrieved higher AOD values, attributable to the increased absorption in the new RI dataset. Furthermore, comparisons with widely cited RI datasets revealed that while the real part of the Asian dust RI showed similar trends, its imaginary part differed markedly in magnitude and shape—reflecting the variability in dust origins. This region-specific RI dataset will help reduce inconsistencies in future studies caused by using RI values from remote sources that may not accurately represent Asian dust characteristics.

Keywords Dust retrieval algorithm · GK-2A geostationary satellite · Optical properties · Refractive index · Asian dust · Radiative transfer model

1 Introduction

Approximately 70% of the atmospheric aerosol mass comprises dust particles (Adebiyi and Kok 2024; Zheng et al. 2023). Although dust supplies nutrients to aquatic ecosystems, such as oceans (Hamilton et al. 2023), primarily through iron-rich components and influences eutrophication and carbon dioxide absorption (Johnson and Meskhidze 2013; Wan et al. 2020; Zhang et al. 2020), it also affects the Earth's radiation budget and contributes to climate change (Kok et al. 2021; Tegen and Lacis 1996). It plays a key role in nucleating ice and water clouds and altering precipitation patterns (Froyd et al. 2022; Kawai et al. 2023). In addition, dust provides the surface required for chemical reactions and is suitable for coating with small anthropogenic pollutants (Dentener et al. 1996). Finally, the decreasing

✉ Sang Seo Park
sangseopark@unist.ac.kr

1 Department of Civil, Urban, Earth, and Environmental Engineering, Ulsan National Institute of Science and Technology (UNIST), Ulsan 44919, Republic of Korea

2 Research & Management Center for Particulate Matters at the Southeast Region of Korea, Ulsan National Institute of Science and Technology (UNIST), Ulsan 44919, Republic of Korea

3 Earth System Division, National Institute for Environmental Studies, Ibaraki 305-0053, Japan

4 Department of Astronomy and Atmospheric Sciences, Kyungpook National University, Daegu 41569, Republic of Korea

visibility and air quality caused by dust (Baddock et al. 2014) play an important role in human lives (Soleimani et al. 2016). Dust storms are quite prevalent in East Asia during spring. Although in recent years, the number of dust events in fall and winter has also increased, likely due to the climate change (Ahn et al. 2024), studies by Yu et al. (2020) and Wu et al. (2022) have demonstrated a decreasing interannual trend in Asian dust activity as reflected in aerosol optical depth (AOD). Thus, tracking and monitoring these phenomena is crucial. Despite the existence of several techniques for dust monitoring, the two major types of remote-sensing technologies are ground-based and space-based methods (Ma et al. 2011).

While ground-based methods provide high-accuracy measurements, they suffer from low spatial resolution due to the scattered and uneven distribution of stations. To address this limitation, satellite remote sensing covers vast areas with a high temporal resolution (Zhang et al. 2024a, b). In satellite-based observations, the AOD is one of the most essential parameters for aerosol retrieval because it can quantify aerosol loading in the atmosphere (Fraser and Kaufman 1985; Lee et al. 2011; Xia et al. 2019). AOD includes contributions from various aerosol types, such as dust, anthropogenic pollutants, sea salts, biomass burning, volcanic ash, haze, etc. As different aerosols have varying impacts on air quality and climate, it is important to separately retrieve AOD data for specific aerosol types. Dust AOD (DAOD) refers to the aerosol optical depth specifically focused on dust, distinguishing it from other aerosol classifications (Chen et al. 2024; Shin et al. 2023; Wang et al. 2020).

Polar-orbit and geostationary satellites (GEO) are key tools for retrieving AOD using remote sensing (Wei et al. 2020). Polar-orbit satellites provide high spatial and spectral resolution AOD products with comprehensive coverage of the Earth (Cavazzani et al. 2015). However, they cannot produce high temporal resolution owing to relatively long revisit time. While Dust transport is generally more homogeneous than cloud dynamics, several studies suggested that a network of polar-orbiting satellites can still capture dust events effectively on event-by-event basis (Hsu et al. 2013; Prospero et al. 2002). Nevertheless, maintaining such a constellation entails significantly higher operational costs and more complex mission design (Macdonald et al. 2014). In contrast, geostationary satellites synchronized with the Earth's rotation remain approximately in the fixed position relative to an observer on Earth (Takenaka et al. 2020). Due to their nearly continuous monitoring and measurement potential, GEO satellites are ideal for dust detection and retrieval (Masuda et al. 2002).

Shortwave reflectance is widely used in AOD retrieval; however, it is considerably uncertain over high-albedo surfaces, such as deserts, and is available only during the daytime (De Paepe and Dewitte 2009; Ji et al. 2024; Letu et al. 2020). Longwave radiance, on the other hand, have advantages due to their 24-hour observation availability, minimum interaction with fine-mode dominated aerosols such as anthropogenic pollutants, and the capability of dust detection over bright surfaces such as deserts and snow (Ackerman 1997; DeSouza-Machado et al. 2010; Dunion and Velden 2004; Klüser et al. 2011; Liu et al. 2013). Thus, remote sensing in the thermal infrared (TIR) is strongly recommended to complement shortwave solar measurements. Although TIR observations have proven extremely valuable in extracting dust aerosol optical properties, discrepancies in this part of the electromagnetic spectrum for DAOD retrieval compared with Visible and near infrared (NIR) are relatively large (Kim et al. 2024).

Previous studies have shown that the accurate determination of DAOD in the TIR requires a complete understanding of dust distribution vertically and horizontally (Callewaert et al. 2019; Pierangelo et al. 2004), chemical composition, and microphysical characteristics of the dust (Castellanos et al. 2024; Hess et al. 1998; Sokolik et al. 1998; Wang et al. 2018). The vertical distribution of dust or Dust Layer Height (DLH), which affects the Brightness Temperature (BT) and the signature of dust particles in TIR, can change the estimated DAOD and cause errors in the results. Furthermore, the chemical composition and microphysical properties, through alterations in the optical interaction of dust aerosols, greatly impact DAOD retrieval in the TIR. Different factors affect the chemical composition, such as the source of dust, pathways, and various interactions during transport. Thus, accurately determining DLH and chemical composition is essential for improving dust retrieval algorithms, radiative budget studies, weather and climate modeling, and understanding tropospheric interactions (Kylling et al. 2018). Several studies have estimated DLH and chemical composition of Asian dust using different methods; however, accurate quantitative sensitivity tests of the AOD for these variables have not been adequately addressed (Kylling et al. 2018; Lee et al. 2015; Zeng et al. 2020).

In recent years, considerable efforts have been made to improve dust retrieval algorithms using the GK-2 A Korean GEO satellite. For instance, the polarized optical depth index (PODI) was added to standard brightness temperature difference (BTD) tests (Jang et al. 2022), and the DAOD error was modified using the conversion coefficient in IR by applying a cumulative distribution function (CDF) (Ahn et al. 2024). These algorithms utilize the BTD method to retrieve the DAOD. In these methods, accurate determination of the optical properties of dust that connect radiance and BT to the DAOD is considerably important. However, to the best of our knowledge, the optical properties of Asian dust in the TIR spectrum based on observations have not been adequately addressed in previous studies.

The bulk properties of Asian dust remain largely uncertain owing to variability in dust origin and compositions, differing analytical approaches, and limited sample availability (Jeong 2008; Jeong and Nousiainen 2014). These limitations introduce errors and biases in retrieving physical and optical properties, ultimately affecting the estimated DAOD. Unrealistic assumptions can lead to inaccurate results, diminished model reliability, misinterpretation of data, biased predictions, and failure to capture the true variability of real-world dust events. These challenges highlight the need for dust retrieval algorithms that incorporate region-specific mineral dust properties, particularly those derived from observations.

This study addresses two key challenges in TIR dust retrieval using geostationary satellites. Its most distinctive contribution is the development of a region-specific refractive index dataset for Asian dust, derived from long-term mineralogical composition data collected in South Korea. The mineralogically derived refractive index, calculated using a fraction-weighted mixing approach and established mineral-specific refractive index datasets, better captures the regional characteristics of Asian dust than the generalized or idealized values commonly used in previous retrieval algorithms. This new dataset is integrated into the TIR dust retrieval algorithm for the GK-2 A satellite to enhance the accuracy of DAOD estimation. While not based on direct optical measurements, this approach narrows the gap between theoretical assumptions and the mineralogical realism of East Asian dust. Second, to investigate the effects of DLH on DAOD retrieval accuracy, we compared the results of sensitivity tests according to the performance of two numerical weather prediction (NWP) models (Asian Dust Aerosol Model 3 (ADAM3) and Unified Model (UM)) and a fixed layer height approach. This study opens up several avenues for future research that aim to bridge the discrepancies between retrieved and observed DAOD.

The remainder of this paper is organized as follows: Sect. 2 describes the data sources and methodology employed for the study. Section 3 outlines the algorithm, details the chemical and optical properties, and the construction of Look-Up Tables (LUTs) using the Radiative Transfer Model (RTM). Section 4 presents the results and provides a comprehensive discussion. Finally, Sect. 5 concludes the paper and summarizes the key findings and implications.

2 Data and Methodology

2.1 Geostationary Korea Multi-Purpose Satellite–2 A (GK-2 A)

GK-2 A is a next-generation geostationary meteorological satellite developed by the National Meteorological Satellite Centre (NMSC) of Korea Meteorological Administration (KMA). The GK-2 A was launched on December 5, 2018, and the data was officially available on July 25, 2019. The Advanced Meteorological Imager (AMI) onboard GK-2 A, using 16 channels (Table 1), improves the radiometric, spectral, and spatial resolution of observations compared to the previous Korean geostationary satellite, Communication, Ocean, and Meteorological Satellite (COMS), with just five channels. Improved spatial resolution (0.5–2 km) in addition to enhanced temporal resolution (10-minute full disk, 2-minute local area scan intervals) increased the meteorological products to 52, significantly more than the 18

Table 1 Spectral characteristics of GK-2 A/AMI bands, including their center wavelengths, bandwidths, and Spatial resolutions. Note: data from the National meteorological satellite center (NMSC), Korean meteorological administration (KMA)

Index	AMI Bands	Center wavelength Spec. Min	Max	AMI Center Wavelength (μm)	Bandwidth Max (μm)	Resolution (km)
1	VIS0.4	0.431	0.479	0.4702	0.075	1
2	VIS0.5	0.5025	0.5175	0.5086	0.0625	1
3	VIS0.6	0.625	0.66	0.6394	0.125	0.5
4	VIS0.8	0.8495	0.8705	0.863	0.0875	1
5	NIR1.3	1.373	1.383	1.374	0.0375	2
6	NIR1.6	1.601	1.619	1.6092	0.075	2
7	IR3.8	3.74	3.96	3.8316	0.5	2
8	IR6.3	6.061	6.425	6.2104	1.038	2
9	IR6.9	6.89	7.01	6.9413	0.5	2
10	IR7.3	7.258	7.433	7.3266	0.688	2
11	IR8.7	8.44	8.76	8.5881	0.5	2
12	IR9.6	9.543	9.717	9.621	0.475	2
13	IR10.5	10.25	10.61	10.3539	0.875	2
14	IR11.2	11.08	11.32	11.2285	1	2
15	IR12.3	12.15	12.45	12.3651	1.25	2
16	IR13.3	13.21	13.39	13.287	0.75	2

products of COMS, making it a perfect tool for monitoring and tracking rapidly developing phenomena such as dust outbreaks (NMSC: https://nmsc.kma.go.kr/).

East Asia stretches from Central Asia to the western coast of the Pacific Ocean, with arid and semi-arid regions primarily located between China and Mongolia as the main sources of dust emissions owing to weak vegetation cover and strong winds (Amgalan et al. 2017; Lee and Sohn 2011). The Gobi and Taklamakan Deserts are key contributors to dust emissions in this region. Although Taklamakan emitting more frequent but weaker dust events, Gobi Desert is responsible for more severe dust emissions (Mu et al. 2023). Dust outbreaks in this area peak from March through May owing to seasonal mid-latitude cyclones and warm, arid soil (Liu et al. 2024). However, due to climate change, the number of dust storms during colder seasons has recently increased (Ahn et al. 2024). Asian dust, predominantly transported by westerly winds, impacts downwind regions and contributes to visibility reduction, Health issues, and transportation challenges. Although Asian dust constitutes approximately 6% of the global average dust load, it specifically contributes to high-altitude dust layers over the North Pacific and Arctic (Kim et al. 2024). This study covers East Asia from 10° N to 55° N and from 95° E to 160° E (Fig. 1).

2.2 AERONET

The AERONET (https://aeronet.gsfc.nasa.gov) program, led by National Aeronautics and Space Administration (NASA) and international partners, is a global network of standardized sun photometers providing long-term, publicly accessible aerosol data for over 25 years. It offers quality-assured measurements of AOD, microphysical properties, and water vapor across diverse environments (Holben et al. 1998). In this study, Level 2.0 AERONET data, representing the highest quality and most accurate measurements (Dubovik et al. 2000), were utilized from 11 stations located along the transport pathway of Asian dust. Details of these stations are provided in Table S1 of the supplementary information, and their locations are shown in Fig. 1. The AERONET data were employed to investigate the dust particle size distribution during transport across the East Asian region and to identify dusty days using key aerosol parameters—AOD, Ångström Exponent (AE), and Fine Mode Fraction (FMF)—by applying established dust-related thresholds (Eom et al. 2022).

2.3 IASI Metop-A

The MetOp-A satellite launched in 2006 was the first European polar-orbiting satellite designed for operational meteorology, with a primary focus on improving NWP. The Infrared Atmospheric Sounding Interferometer (IASI) is a hyperspectral spectrometer onboard the MetOp-A satellite designed for nadir observations with 2200 km swath width. Using Fourier transform spectroscopy, the IASI retrieves AOD in TIR (AOD_{TIR}) using the LUT method, which has been validated against various reference data (Clarisse et al. 2019; Peyridieu et al. 2013). IASI AOD_{TIR} products are particularly valuable because of the limited officially

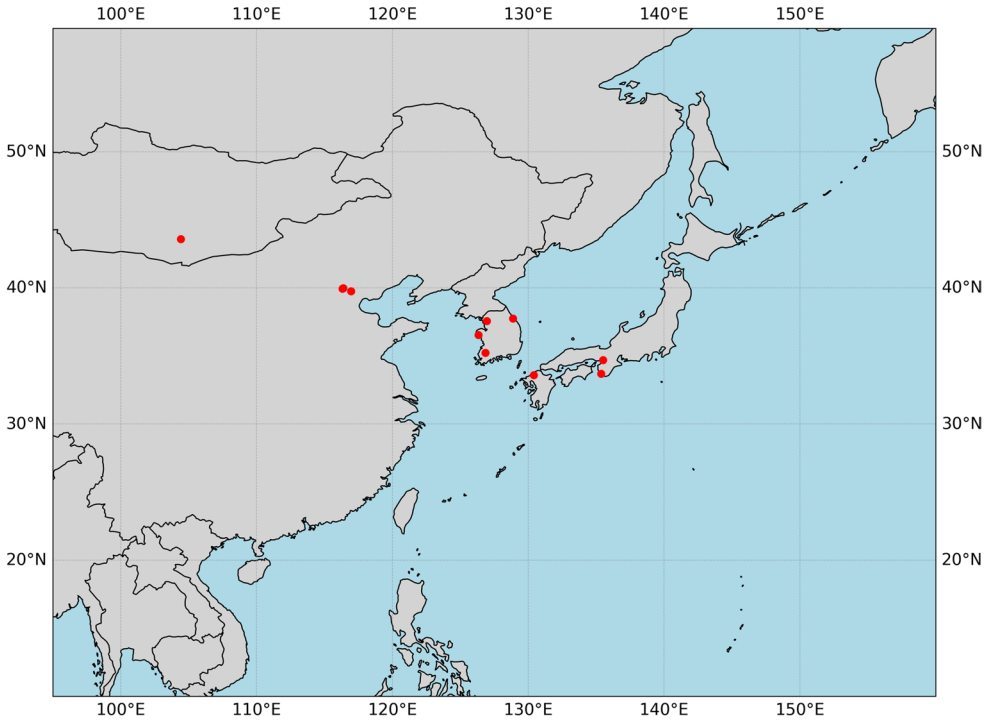

Fig. 1 Study region spanning 10°N–55°N and 95°E–160°E, encompassing key areas along the East Asian dust transport pathway. Red dots mark AERONET stations used to analyze coarse-mode aerosol volume size distributions on dusty days (2015–2024). Stations are located across Mongolia, China, Korea, and Japan, representing source, transport, and receptor regions. The details of the stations are provided in Table S1 of the supplementary materials

published datasets for aerosol retrieval in the TIR spectrum, specifically for dust particles (Zheng et al. 2023). In this study, we relied on the IASI-LMD algorithm L2 data developed by the Laboratoire de Météorologie Dynamique for comparison and analysis, available at (https://iasi.aeris-data.fr).

2.4 Moderate Resolution Imaging Spectroradiometer (MODIS)

MODIS is a key sensor for the Aqua and Terra satellites that provide important information related to the Earth's surface, atmosphere, and space (L'Ecuyer and Jiang 2010). The two main algorithms for MODIS aerosol products are Dark Target (DT) and Deep Blue (DB), which process surface reflectance differently (Bilal et al. 2017). We utilized MODIS Collection 6.1 data from the Terra satellite, specifically Level 2 AOD products. This dataset, which has a spatial resolution of 10 km, was derived from the combined DT and DB algorithms. (https://ladsweb.modaps.eosdis.nasa.gov/). The MODIS aerosol product represents a mixture of various aerosol types and does not provide dust-specific AOD values (Georgoulias et al. 2016). Moreover, the AE, a commonly used parameter to distinguish coarse-mode particles such as dust from fine-mode aerosols (Schuster et al. 2006), is unavailable over land due to high surface reflectance variability and associated retrieval uncertainties in this dataset. To address this limitation and isolate dust-affected regions for our analysis, we adopted two complementary approaches. First, we verified the dominance of dust through ground-based AERONET observations. Dusty days were identified by applying well-established thresholds: AOD > 0.4, AE < 0.7, (Eom et al. 2022) and FMF < 0.4. Second, we selected case study dates that are widely recognized for major dust outbreaks over East Asia declared by KMA. Together, these approaches allowed us to reasonably attribute high AOD values in the MODIS product to dust aerosols, despite the lack of aerosol-type separation in the MODIS dataset itself.

3 Dust Retrieval Algorithm

In this section, we provide details related to the determination of clear pixels, dust detection, LUTs construction, DAOD retrieval, and methods for improving the accuracy of the algorithms used in this study. To perform sensitivity tests regarding the impact of the refractive index customized for Asian dust and various dust layer height determination methods, we must maintain the operational algorithm framework and assumptions to eliminate or at least reduce the effects of other variables on the sensitivity examinations. The details are summarized in Fig. 2.

Clouds can significantly interfere with the DAOD retrieval process in the TIR by exhibiting spectral signatures similar to dust (Zheng et al. 2022). Detection and removal of cloudy pixels to avoid cloud-contaminated pixel errors during retrieval is essential. Dusty pixels were selected for further analysis among the cloud-free pixels. Conventional satellite channels for dust detection include 11.2 μm and 12.3 μm (Ackerman 1997; Chen et al. 2014) as a negative BTD_{11-12} ($BT_{11\mu m}$ - $BT_{12\mu m}$) can be associated with dust load, indicating high DAOD. However, identifying dust over high-albedo surfaces, such as deserts, remains challenging. De Paepe Dewitte (2009) demonstrated that the $BTD_{11-8.6}$ ($BT_{11\mu m}$ - $BT_{8.6\ \mu m}$) is effective method for this purpose. In new GEO satellites, an additional 8.6 μm channel, where dust absorption is strong, is applied to increase the accuracy.

AOD estimation in the TIR region is complex and requires accurate RTM simulations, which depends heavily on well-characterized surface properties (surface temperature and emissivity) and vertical atmospheric profiles (temperature, pressure, water vapor, ozone, CO_2, NO_2, etc.) (Scott and Chedin 1981). All RTM simulations in this study used the U.S. standard atmospheric profile at mid-latitude. Although window channels exhibit minimal interaction with atmospheric gases, the potential influence of water vapor on TIR channels remains a notable concern (Thomas 1987). To assess this impact, we conducted a series of sensitivity experiments by modifying the water vapor content of the US-Standard profile in five steps: −50%, +25%, +50%, +75%, and +100% (doubling) illustrated in Figure S1 in supplementary information to investigate the water vapor effects on BT simulations in RTMs.

The results indicate that the IR 7.3 μm channel exhibits the greatest sensitivity to changes in water vapor, as expected due to its location within a strong absorption band. In contrast, other channels show smaller responses, with BT variations of approximately 0.5 K for the IR 9.6 μm channel and up to 2.5 K for the IR 12.3 μm channel. After applying the BTD calculation, the Maximum residual difference compared to the original profile was reduced to 0.7 K. Overall, although water vapor is an important parameter in the TIR region, the use of BTDs helps to cancel out and minimize its impact. This finding may explain why using regionally averaged water vapor profiles from the European Centre for Medium-Range Weather Forecasts (ECMWF) Reanalysis-5 (ERA5) over clear-sky conditions in East Asia to construct our LUTs did not lead to significant deviations in the retrieval results. Nevertheless, for future refinement, we plan to incorporate pixel-level water vapor profiles from reanalysis datasets such as ERA5 or the Modern-Era Retrospective Analysis for Research and Applications, Version 2 (MERRA-2) to enhance the accuracy of the algorithm.

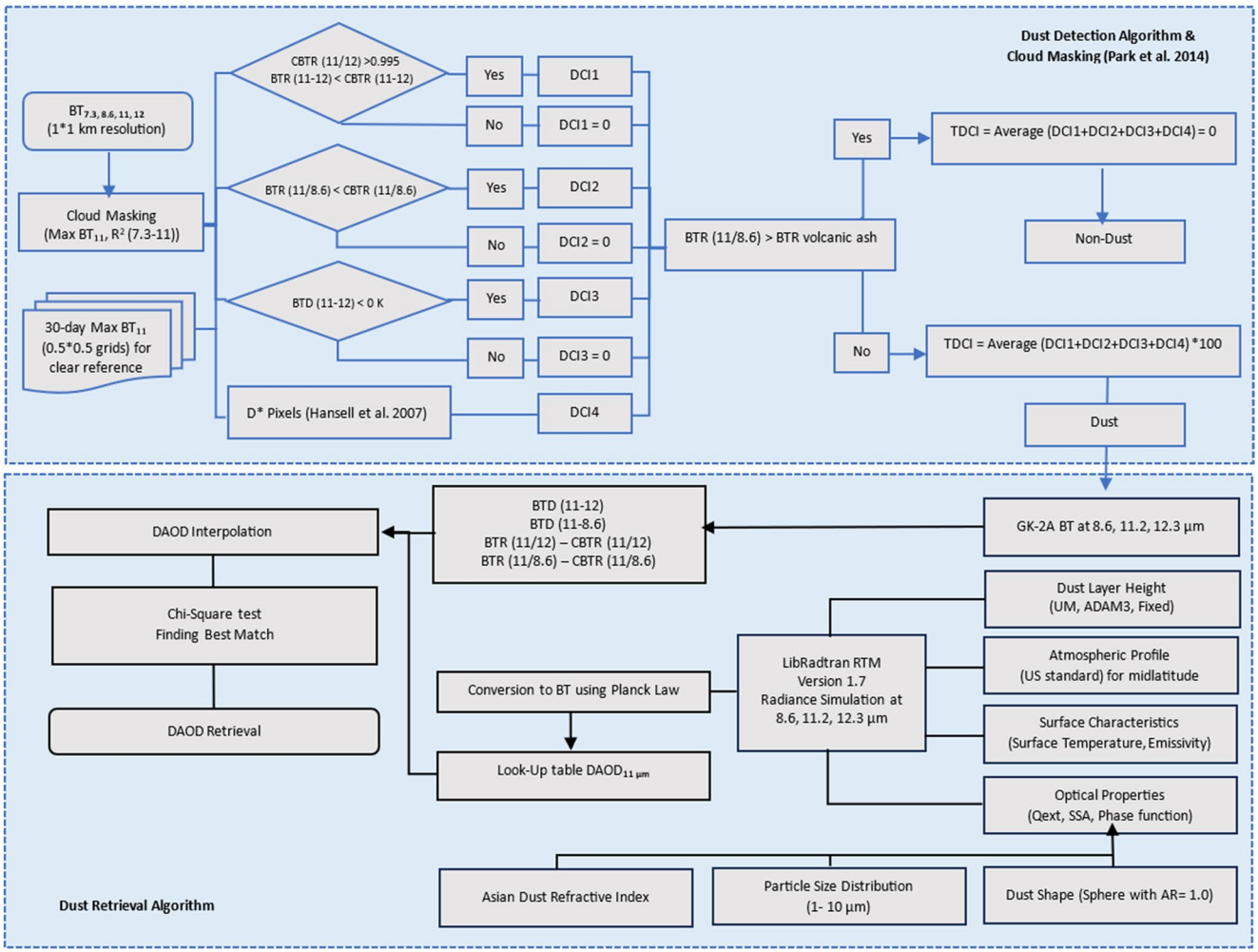

Fig. 2 Flowchart of the dust retrieval algorithm developed in the study, incorporating dust detection and cloud masking steps, based on Park et al. (2014). The algorithm utilizes GK-2 A satellite data to detect and characterize Asian dust events

Background Brightness Temperature (BBT) is defined in this study as the Maximum 11 µm brightness temperature at the top of atmosphere (TOA), observed by the GK-2 A satellite over the previous 30 days under presumed clear-sky conditions, for each 0.5° × 0.5° pixel. BBT is primarily influenced by surface temperature and emissivity (Dash et al. 2002). While surface temperature varies more significantly, surface emissivity also plays an important role in determining observed radiances. Although we assume surface emissivity to be constant in this study for exact alignment by operational algorithm, previous research (Li et al. 2012; Ogawa et al. 2008) has shown that emissivity can vary both spatially and temporally—even over the course of a single day—depending on surface type, moisture content. The main reason this approach was chosen—despite some known limitations—is that it replicates exactly the method used in the current GK-2 A operational dust detection algorithm (Park et al. 2014). Maintaining this method ensures methodological continuity and compatibility, and more importantly, it helps prevent the introduction of uncontrolled biases into sensitivity experiments that could arise from altering key retrieval assumptions.

After a pixel was flagged as dusty, a land/ocean mask and geopolitical boundaries were applied to determine its location within the region of interest. Subsequently, DLH was calculated using the UM- and ADAM3-based models, as well as the fixed DLH method. In addition to the three DLH methods, this study tested the algorithms in operational and updated forms. Table 2 summarizes the retrieval methods and the abbreviations that are used hereafter. The operational methods ('Op') represent the currently used algorithm in the GK-2 A satellite, whereas the updated version ('Up') represents our algorithm with RI designed specifically for Asian dust.

Reference values were stored according to various AOD, wavelengths, DLH, and effective radius (R_{eff}) values in the LUTs. Moreover, interpolation was performed with

Table 2 Summary of dust retrieval methods using different dust layer height determination and their abbreviations used in this study

NWP Model	Operational Algorithm	Updated Algorithm
Unified Model (UM)	Op-UM	Up-UM
ADAM3 Model (AD)	Op-AD	Up-AD
Fixed Height Method (Fix)	Op-Fix	Up-Fix

the LUTs regarding the geometrical parameters. The calculated weights were used to refine the interpolated values and improve accuracy. A Chi-square test was then applied to determine the optimal points at which the LUTs values matched the observed data. Finally, fine-tuning was performed using bilinear interpolation between adjacent points in the LUTs to more precisely determine the parameter values.

Methods and techniques in passive remote sensing are varied. However, microphysical properties cannot be determined completely because of insufficient information regarding radiation. Thus, in several cases assumptions that deviate from reality are unavoidable. As a result, errors occur in retrieving dust aerosols, and a large bias exists between observations and models.

3.1 Chemical Composition and Refractive Index (Chemical and Optical Properties)

Optical properties illustrate how particles interact with light and must be determined along with their horizontal and vertical distributions, chemical compositions, and microphysical characteristics. The key optical properties include the extinction coefficient (Q_{ext}), single-scattering albedo (SSA), and asymmetry parameter (ASYM). Accurately estimating these properties requires precise information on the particle size distribution (PSD), refractive index (RI), and dust particle shape. The refractive index, primarily determined by mineralogical and chemical composition of dust, plays a key role in governing the particles' ability to scatter and absorb radiation. Although particle size and shape significantly influence scattering and absorption behavior, they do not directly define the refractive index itself (Kong et al. 2024).

The chemical composition of dust varies significantly due to differences in source regions and alterations along transport pathways (Wang et al. 2022). Previous studies have confirmed the distinct chemical composition variation of Asian dust compared with other dust sources and the contrast between long-range transported dust and its origin (Baldo et al. 2020; Di Biagio et al. 2017; Jeong 2020). Bhatia & Crook (1986) found that Asian dust and Gobi Desert soils largely originated from the same source rocks. Similarly, Jeong (2020) reported that the Gobi Desert is the main source of Asian dust collected persistently in the Korean Peninsula owing to similarities in the main and trace element components.

Table 3 Volume fractions and standard deviations of mineral components used for the refractive index calculation. Adapted from (Jeong 2020), based on 25 Asian dust samples collected during 2005–2018 in South korea.

Mineral	Volume Fraction (%)	Standard Deviation (%)
Quartz	20.6	3.7
Plagioclase	12.4	2.2
K-feldspar	5.1	1.9
Illite	19.4	4.5
Illite + Smectite	22.6	9.3
Chlorite	4.0	1.1
Kaolinite	2.1	0.6
Calcite	5.1	0.8
Dolomite	1.5	0.4
Gypsum	5.0	4.4

Although the bulk properties of Asian dust are largely unknown due to complexity of dust compositions, diverse origins, different analytical methods, and insufficient sample availability, reliable data on dust's chemical and optical properties are necessary to improve Earth System Models (ESMs) (Jeong 2008; Jeong et al. 2014; Kanayama et al. 2002; Leinen et al. 1994; Shi et al. 2005). In this study, we calculated the refractive index of Asian dust based on mineralogical analyses of 25 samples collected during 14 dust outbreaks over the Korean Peninsula between 2005 and 2018, as reported by (Jeong 2020). Table 3 summarizes the average mineralogical composition and standard deviations of these samples, which were used as volume fractions in constructing the bulk complex refractive index for Asian dust.

Capelle et al. (2014) demonstrated that, in the worst-case scenario, using an inappropriate refractive index dataset could result in up to 25% discrepancies in estimating the radiance at the TOA. While the refractive index is a key optical property in the TIR region, its influence on radiative characteristics is strongly dependent on the wavelength. Although the 11–12 μm region lacks strong resonant peaks in most mineral compositions and is therefore relatively insensitive to changes in the refractive index (Y. H. Zhang et al. 2024a, b; Zheng et al. 2022) quartz and clay minerals—key constituents of Asian dust—exhibit pronounced spectral resonance in the 9–10 μm region (Di Biagio et al. 2017). The refractive index is a complex number describing the material compositions' optical effects (Castellanos et al. 2024; Sorensen et al. 2019). The complex index of refraction can be written as:

$$\widetilde{n}(\lambda) = n(\lambda) + ik(\lambda)$$

Where $\tilde{n}$ represents the complex refractive index as a function of wavelength (λ), n is the refraction index, and k is the absorption index. Information on the refractive index of Asian dust, specifically in the TIR region, remains limited (Alalam et al. 2024; Bi et al. 2020). The complex refractive index of the Asian dust mineral components was derived from previous studies and the Aerosol Refractive Index Archive (ARIA) (https://eodg.atm.ox.ac.uk/ARIA/data?Minerals/) provided by the Department of Physics at the University of Oxford. The references used to obtain the refractive indices of the minerals in this study are summarized in Table 4.

Mineralogical analyses of Asian dust particles collected from Seoul, Korea, and Beijing, China, revealed that the compositions were dominated by clay silicates and quartz, followed by feldspar and calcite, including dolomite, along with trace amounts of amphibole and gypsum (Jeong 2008). Mineral dust exhibits regional variability in the ratios and components of its major and trace elements (Kandler et al. 2011; Kok et al. 2021; Sokolik and Toon 1999). The most abundant mineral in Asian dust particles is quartz. This anisotropic (birefringent) mineral splits incident light into two rays (ordinary (o-ray) and extraordinary (e-ray) with moderately different paths. The refractive index of quartz was obtained from the ARIA dataset (Kitamura et al. 2007). In this study, we calculated the refractive indices for all birefringent minerals using the average o-ray and e-ray data. He et al. (2016) illustrated that deposits in samples from the Chinese Loess Plateau, specifically from the central part of China, represent the complete mixing of various dust sources. No anorthite was detected among the analyzed plagioclase subspecies, and the amount of bytownite was negligible (0-0.3%). Albite was the most abundant subspecies, accounting for 14.73–16.32% of the plagioclase samples. The optical properties of albite obtained by Mutschke et al. (1998) represents the plagioclase group. Orthoclase, the most common K-feldspar, was selected as an appropriate representative of this group; comprehensive data on its optical properties were provided by Arnold et al. (2014). In several cases, such as calcite ($CaCO_3$) reported by (Posch et al. 2007) in the ARIA dataset, the n and k were only reported at 200 K and 300 K. To improve the accuracy, we interpolated and obtained refractive indices at 268.5 K and then averaged o-ray and e-ray. This temperature represents the average temperature from the surface to 6 km, where 95% of the vertical mass profile of dust is located, based on the annual average (Kim et al. 2024). The optical constants for clay minerals (illite, smectite (montmorillonite), kaolinite), and dolomite were obtained from Querry (1987) from ARIA datasets within the 2.5 to 100 μm spectral range. For illite-smectite composite particles, the effective refractive index was calculated using an illite-to-montmorillonite ratio of 1:5, as described by Shi et al. (2005). The real and imaginary parts of chlorite and gypsum were sourced from Mooney and Knacke (1985) and Roush et al. (2007), respectively. The real and imaginary parts for components of Asian dust over a spectral range of 5.0 μm to 16.0 μm are shown in Fig. 3.

Table 4 Information on mineral components relevant to Asian dust including components, references, wavelength ranges, and publication years. Note: it includes data from the aerosol refractive index archive (ARIA) maintained by the department of physics at the university of Oxford

Components	Reference	Wavelength Range (Min-Max) (μm)	Published Year
Calcite	ARIA (Posch et al.)	2.0-100	2007
Chlorite	Knacke	2.5–100	1985
Dolomite	ARIA (Querry)	2.5–100	1987
Gypsum	Roush et al.	0.4–15	2007
Illite	ARIA (Querry)	2.5–100	1987
Kaolinite	ARIA (Querry)	2.5–100	1987
K-Feldspar	Arnold et al.	2.4–40	1998
Plagioclase	Mutshke et al.	6.68-85	2014
Quartz	ARIA (Kitamura)	6.165-50	2007
Smectite (Montmorillonite)	ARIA (Querry)	2.5–100	1987

Mineral dust is composed of internal and/or externally mixed aerosol particles. Several methods are available to determine the effective optical constants of particles in a mixture of different components. In this study, we used the fraction-weighted average method to calculate the refractive indices of the constituent minerals as follows:

$$m = \sum_{j=5}^{16} \mathrm{f}_j \mathrm{m}_j$$

Where m is refractive index (n+ik), f_j is volume fraction, and m_j is complex refractive index (j in range 5 to 16 μm). A key assumption of this study was that Asian dust particles consist of externally mixed minerals, meaning that the individual constituent particles are composed of only one species. However, natural particles are chemically and mineralogically heterogeneous. In addition, chemically homogeneous particles can be coated with anthropogenic pollutants (Kandler et al. 2011; Sobanska et al. 2012). Although these considerations are necessary, further investigations in this area are beyond the scope of this study.

In more complex methods, the effective dielectric constants of the composites are used. Whenever inclusion minerals are embedded in homogenized matrix minerals, the Maxwell-Garnett method is used (Garnett and Larmor 1997; Sokolik and Toon 1999), whereas when the matrix and inclusions cannot be distinguished, the Bruggeman approximation (Bruggeman 1935) is helpful. Lee and Park (2014) showed that the real part of refractive indices

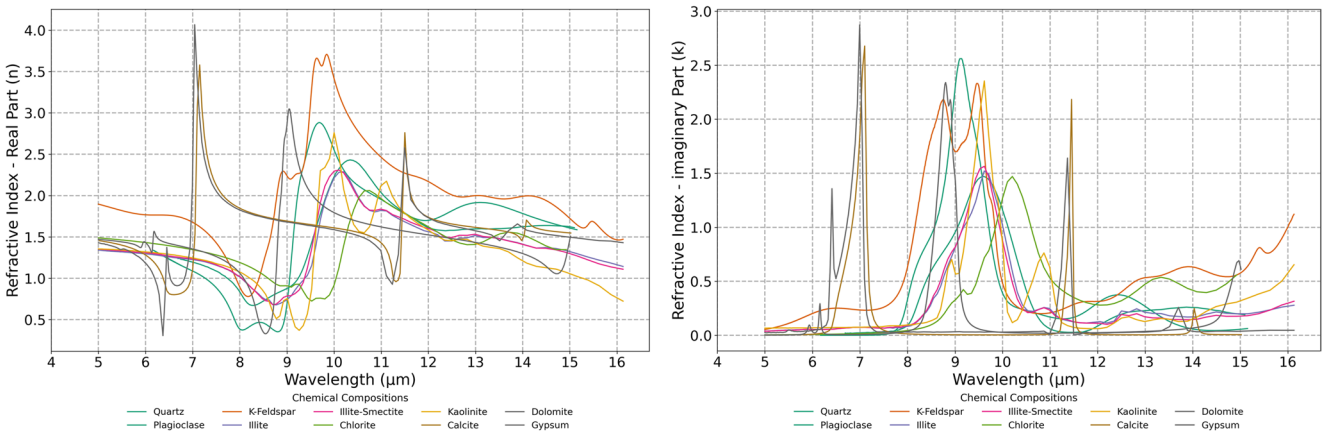

Fig. 3 Refractive indices of mineral components in Asian dust particles across the 5.0–16.0 μm wavelength range. The plot highlights the variations in the real part (left) and imaginary part (right) of refractive index values for each mineral

calculated using the three methods mentioned above (i.e., fraction-weighted average, Maxwell-Garnett, and Bruggeman) had identical results. The differences were so small for the imaginary part except in 7.09 μm and 8 μm. Furthermore, the performance of the Maxwell-Garnett and Bruggeman models deteriorates as the size parameter increases, and dust particles are considered as large aerosols (Nousiainen 2009).

3.2 Dust Shape and Size Distribution

The dust particles are irregularly shaped with non-spherical grains. The Aspect Ratio (AR), the ratio of the longest dimension to the intermediate dimension, is a commonly used index for describing non-spherical particles. Jeong et al. (2016) demonstrated that the median AR for Asian dust is 1.72, and the standard Height-to-Width Ratio (HWR) was 0.35. In contrast to African dust with AR and HWR of 1.6 and 0.6, respectively, Asian dust typically exhibits more elongated and narrower dust particles (Castellanos et al. 2024).

Dust particles are often assumed spherical in Many RTMs simulations of the TIR region. This treatment is justified by the completely different behavior of dust particles at wavelengths below 6 μm, where the scattering process dominates, in contrast to wavelengths longer than 6 μm, where the absorption is dominant. Non-sphericity significantly impacts light scattering rather than absorption, and this effect is not considerable in the TIR region (above 6 μm) where absorption is main process (Di Biagio et al. 2017). Moreover, to determine the single-scattering characteristics in the TIR region, the role of the refractive index far outweighs that of the particle geometry (Nousiainen 2009). In this study, we used a spherical shape (AR = 1.0), similar to the operational algorithm, to hinder the impact of the shape on the sensitivity tests.

Pierangelo et al. (2004) argued that compared with AOD or Aerosol Layer Height, the impact of size distribution is not strong enough to introduce substantial bias. However, more recent studies (Adebiyi and Kok 2020; Ryder et al. 2018) have emphasized that climate models often underestimate the contribution of coarse-mode dust—up to a factor of four—leading to significant biases in radiative effect estimations. In the operational algorithm, the particle size distribution is not retrieved directly; instead, a monomodal lognormal size distribution is assumed and defined as:

$$\frac{dV}{d\ln r} = \frac{V_0}{\sqrt{2\pi}\,\ln\sigma}\exp\left(-\frac{(\ln r - \ln r_g)^2}{2\,ln^2\,\sigma}\right)$$

where $\frac{dV}{d\ln r}$ is the volume size distribution, r_g is the geometric mean radius, σ is the geometric standard deviation, and V_0 is the total particle volume. A dynamic range of effective radii (1–10 μm) is explored to construct the LUT. For each effective radius value within this range, extinction coefficients and other optical properties are computed using Mie theory, based on pre-calculated refractive index values and a fixed geometric standard deviation (σ). These optical properties are then used in radiative transfer simulations to generate BT responses for varying AODs. The operational retrieval primarily uses the $BT_{11\mu m}$ to estimate AOD, with the best-fit solution chosen by comparing observed and simulated BTs. Due to the limited degrees of freedom in a single-channel TIR retrieval ($BT_{11\mu m}$), particle size cannot be retrieved simultaneously. Therefore, the LUT is constructed over the fixed size range to accommodate potential size effects without explicitly retrieving them.

In the updated algorithm, we retained the same dynamic size range for constructing the LUTs and retrieving AOD. However, to investigate dust particle size distribution more thoroughly, we analyzed AERONET data from 11 stations across the East Asian dust transport pathway for the period

2015–2024. Dusty days were identified using the following thresholds: AOD > 0.3, FMF < 0.4, and AE < 0.7. High AOD values indicate elevated aerosol concentrations, while low FMF and AE values signify the dominance of large particles such as dust. For regional comparison, the East Asian domain was divided into three subregions: Mongolia–China, South Korea, and Japan. The results of these regional comparisons and particle size analyses are presented and discussed in detail in the Results and Discussion section.

3.3 Radiative Transfer Model Calculations

The Radiative Transfer Equation (RTE) is a fundamental equation that describes the light intensity variation in a medium, accounting for scattering, absorption, and emission. Based on this equation and using scattering models, RTMs simulate TOA radiance, which is essential for retrieving aerosol properties. There is always a trade-off between accuracy, complexity, and computational expenses, on which choosing RTMs is dependent on. In this study, we employed the Library for Radiative Transfer (libRadtran) version 1.7, a widely used software package for radiative transfer calculations (Mayer and Kylling 2005). Discrete Ordinate Radiative Transfer (DISORT), the most cited radiative transfer code in Earth science for handling dust absorption and scattering calculations, was utilized (Stamnes et al. 1988), which developed in the 1980 s and is still widely used.

The LUT approach was used to accelerate the dust retrieval process. LUT-based algorithms comprise two main steps: forward simulation and an inversion process based on various variables. Highly sensitive variables must be calculated with high accuracy and high resolution during LUT construction. In contrast, variables with low or negligible sensitivity are typically considered with a coarser resolution and fixed, respectively. We calculated the radiance at TOA for three TIR channels (8.6, 11.2, and 12.3 μm) using libRadtran and stored in LUTs. The inputs used in the RTM are listed in Table 5.

Table 5 Input parameters and their value ranges were used to generate Look-Up tables (LUTs) for dust retrieval in the thermal infrared spectrum

Parameters	Number of Values	Values/Range
Wavelength	3	8.6, 11.2, 12.3
AOD	10	0, 0.2, 0.4, 0.6, 0.8, 1.0, 1.2, 1.4, 1.6, 1.8 (in 8.6 μm)
Effective Radius	10	1–10 μm (1 μm intervals)
Dust Layer Height	10	1–10 km (1 km intervals)
Solar Zenith Angle (SZA)	9	0–80 degrees (10-degree intervals
Viewing Zenith Angle (VZA)	17	0–80 degrees (5-degree intervals)
Relative Azimuth Angle (RAA)	18	0–170 degrees (10-degree intervals)

4 Results and Discussion

4.1 Refractive Index of Asian Dust

Accurate dust aerosol retrieval in East Asia requires a region-specific RI dataset. However, most current satellite retrievals rely on RI values derived from remote regions such as Germany (Volz 1972), Barbados (Volz 1973), or globally averaged datasets like Optical Properties of Aerosols and Clouds (OPAC) (Hess et al. 1998) as these are among the most cited references in remote sensing, which may introduce significant biases. Highwood et al. (2003) showed that in the TIR region even small changes in the imaginary part of the RI causes considerable alterations in the modeled brightness temperature. Di Biagio et al. (2017) conducted a comprehensive study comparing 19 soil samples from eight global dust sources, including the Gobi Desert to derive their complex refractive indices. Figure 4 compares the refractive indices obtained in this study (ERML 2025) and the established datasets. The whole data related to the refractive indices (including text, pdf, and excel files) used in this study are provided in Supplementary materials.

The results show that while the real part of the refractive index (n) follows a broadly similar trend across datasets with different magnitudes, the imaginary part (k) varies significantly in both shape and magnitude—indicating differences in chemical composition and dust origin. Our study reveals notably higher k values for Gobi Desert dust, a key source of East Asian aerosols, compared to existing datasets. This contrasts with Di Biagio et al. (2017), who reported lower k values for Gobi samples. They also Linked peak absorption in the 8–12 μm range to the PSD, noting stronger absorption for samples rich in super-micron particles. Thus, the k-value peak for Asian dust in our study highlights the need for more accurate investigations of the PSD, specifically in downwind areas. The elevated k in our dataset may reflect the high clay (48%) and quartz (20%) content in Asian dust, which have strong absorption bands at 9.6 μm and 9.2 μm, respectively.

The Kramer-Kronig (K-K) relationship, rooted in electromagnetic theory, provides a way to test the physical validity and internal consistency of complex refractive index datasets by linking the real part (n) to the imaginary part (k) across the full spectrum (0–∞) through integral transforms (Kam 1983). Accurate application requires data over a broad wavelength range, as omitting parts can lead to skewed results (Segal-Rosenheimer and Linker 2009). Since this study is Limited to 6–14 μm, the K-K relationship could not be applied. Future work will extend the spectral range to enable proper validation.

Unlike Di Biagio et al. (2017), who derived RI values from a limited number of short-term samples collected near source regions, our study is based on long-term chemical

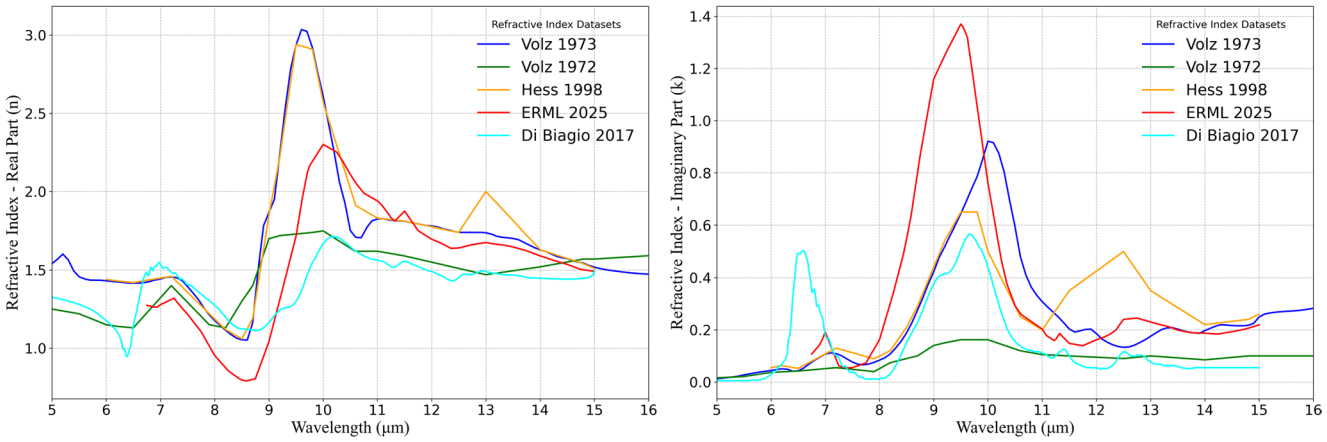

Fig. 4 Comparison of the real part (left) and imaginary part (right) of the refractive index for dust from various global sources, including Hess (1998), Volz (1972, 1973), Di Biagio et al. (2017) and this study (ERML 2025). The real part in the thermal infrared region shows a similar trend across all datasets, with different magnitudes. In contrast, the imaginary part exhibits significant differences in shape and magnitude, reflecting variations in dust absorption properties

composition data from downwind locations. They argued that coarse particle settling, minimally affects longwave absorption due to stable chemical ratios during transport, they also acknowledged spatial variability in the k-value even in the same region, which supports the need for broader sampling. Relying solely on source-region data may introduce biases in global modeling and remote sensing applications.

Despite this study's contribution in addressing those gaps, available long-term datasets on Asian dust composition remain limited. These findings align with prior work such as Lee and Park (2014), who used Bruggeman's rule under internal mixture assumptions. By incorporating long-term observational data on the chemical composition of dust, this study offers a more realistic RI for East Asian dust, helping reduce DAOD retrieval errors and bridging the gap between model estimates and satellite observations.

4.2 Dust Layer Height (DLH)

DLH refers either to the real height—defined by the physical boundaries of the dust layer (i.e., top and bottom altitudes)—or to the effective height, representing the altitude where the total dust burden can be assumed to reside for radiative transfer purposes (Kylling et al. 2018). For DLH determination, we used the ADAM3 and UM models. Additionally, we investigated the fixed DLH method proposed by Li et al. (2024), who suggested that DLH generally resides between the surface and 5 km for total aerosols and is reduced to 3 km for dust particles. ADAM3 estimates DLH using the cumulative extinction method. In this approach, the vertical dust extinction profile is used to identify the altitude at which the cumulative extinction reaches 50% of the total column, representing the central layer height. This study assumes that the dust is concentrated within a single, homogeneously distributed layer to simplify calculations. However, Kylling et al. (2018) noted that, Typically, 50% of the column-integrated extinction lies below the geometric mean height, indicating a lower atmospheric concentration of aerosols. This indicates that dust particles are typically concentrated in the lower part of the vertical profile and that a symmetric distribution May not fully represent real atmospheric conditions. Therefore, the assumed Gaussian profile serves as a simplification and May not capture the full complexity of dust vertical structures. On the other hand, the UM model provides the temperature vertical profile in 70 levels from surface to around 84 km. the algorithm finds the altitude where UM model temperature matches the observed BT (effective height). Figures 5 presents the average DLH values, calculated from cloud-free, dusty pixels over China, Korea, and Japan on 28 March 2021, using three different methods.

The fixed DLH model consistently assumes a 3 km Height with a 1 km standard deviation. In contrast, both ADAM3 and UM show regional variability and reveal important vertical structure characteristics. Over China, both models indicate elevated DLHs (ADAM3: 3.08 km; UM: 4.28 km), likely due to uplift of dust into the free troposphere during long-range transport. The extinction profile over China shows a more gradually decreasing vertical trend, whereas Korea and Japan exhibit more pronounced extinction peaks. As dust is transported eastward, the DLH decreases from China to Japan. However, the UM model still estimates higher DLH values than ADAM3 across all regions. The ADAM3-based DLH difference between Korea and Japan is approximately 0.5 km, with lower extinction magnitudes observed toward the downwind region, consistent with reduced aerosol loading during transport.

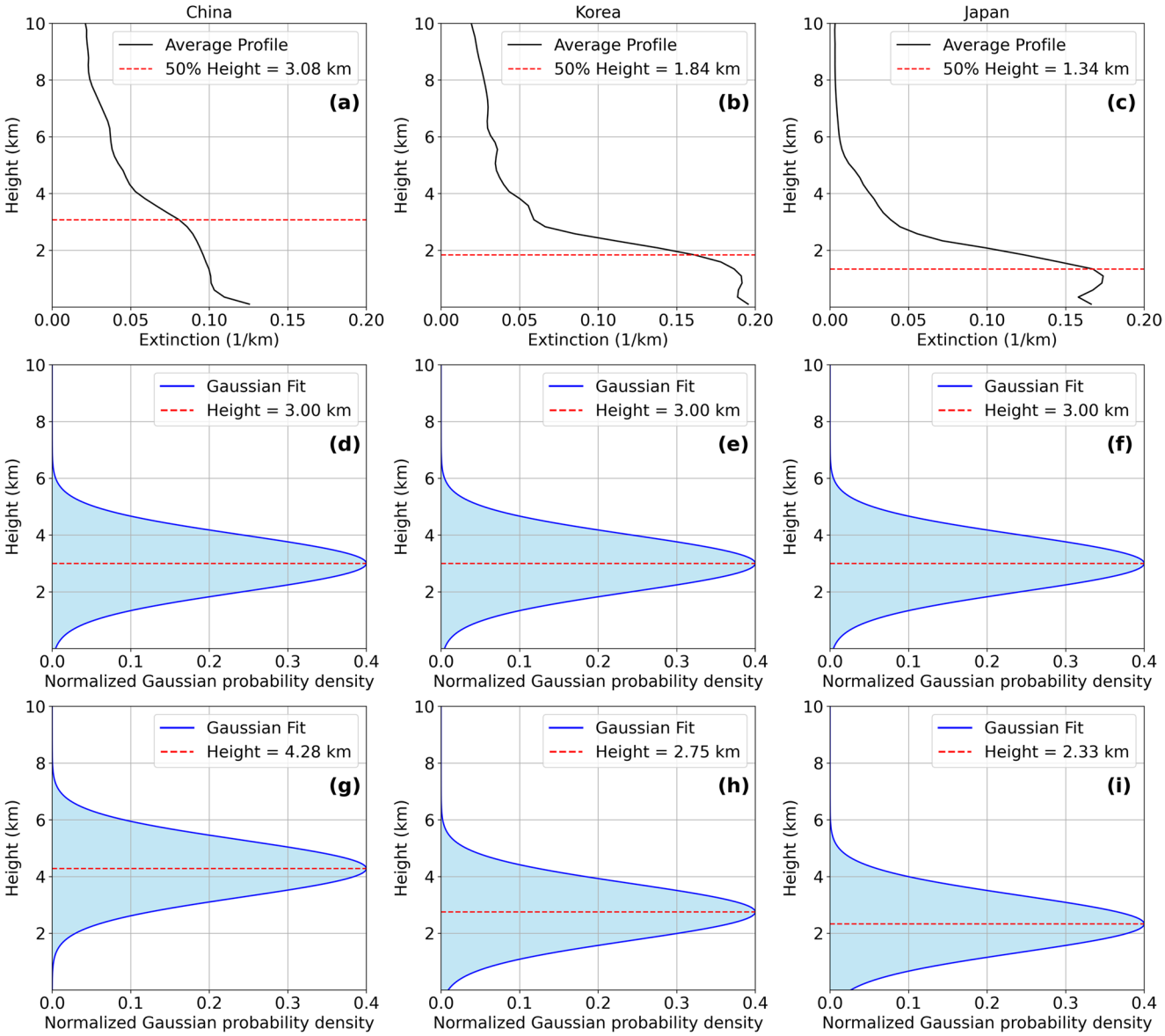

Fig. 5 Vertical distributions of DLH over East Asia on 28 March 2021 for China (left), Korea (center), and Japan (right). Top row (**a–c**): DLH estimated from the ADAM3 model using the 50% cumulative aerosol extinction method. Middle row (**d–f**): Fixed Gaussian model centered at 3.0 km (σ = 1.0 km). Bottom row (**g–i**): DLH derived from the Unified Model (UM), modeled with a Gaussian profile centered at the UM-based height (σ = 1.0 km)

4.3 Dust Size Distribution

A regional analysis was conducted using 980 valid observations collected on dusty days from 11 AERONET stations along the Asian dust transport pathway between 2015 and 2024 as illustrated in Fig. 6.

The effective radius is a key parameter for describing the size distribution of particles and is calculated using the following formula:

$$r_{eff} = \frac{\int r^3 n(r)\, d(r)}{\int r^2 n(r)\, d(r)}$$

Where r is particle radius, $n(r)$ is the number distribution, and dr is the bin width. The R_{eff} and geometric mean radius (R_g) of coarse-mode particles exhibit a gradual decrease along the transport path—from Mongolia and northern China ($R_{eff} \approx 5.27$ μm, $R_g \approx 2.55$ μm) to Korea ($R_{eff} \approx 5.22$ μm, $R_g \approx 2.29$ μm), and further to Japan ($R_{eff} \approx 5.16$ μm, $R_g \approx 2.13$ μm). This spatial gradient aligns with expectations from gravitational settling and aerosol aging during long-range transport. A similar pattern is observed in the frequency of dusty days, with the highest number of valid cases in the source region (Mongolia–China: 512), followed by Korea (309) and Japan (159).

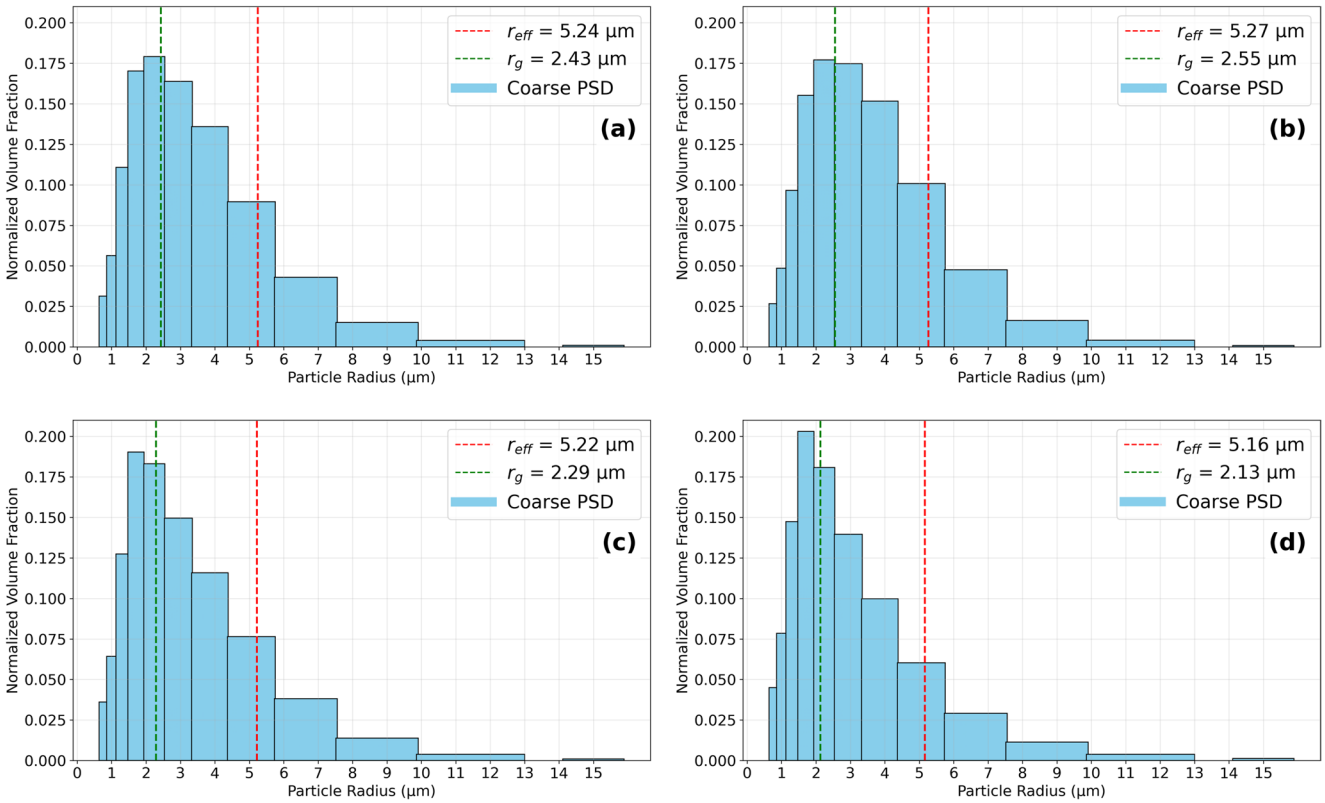

Fig. 6 Normalized coarse-mode aerosol volume size distributions from 11 AERONET stations (Level 2.0) on dusty days (2015–2024) across East Asia. Bars indicate normalized volume fractions (unitless) across non-uniform radius bins within the coarse mode (0.6–15 μm), following AERONET's native logarithmic spacing. Red and green dashed lines represent the mean R_{eff} and geometric radius (Rg), respectively. Fine-mode particles (<0.6 μm) are excluded due to Limited thermal infrared relevance. Final Bin is truncated at 15 μm per retrieval limits

While some spatial variability exists, the overall range in size parameters is relatively narrow— R_{eff} from 5.16 to 5.27 μm and R_g from 2.13 to 2.55 μm. This modest variation suggests that a regionally representative, fixed size distribution can be used in LUT-based retrievals without significant loss of accuracy, particularly when paired with an appropriate standard deviation (σ). Given the strong radiative sensitivity of TIR channels to coarse-mode particles, even small size changes can impact retrievals. However, the observed consistency supports a simplified yet physically realistic parameterization, balancing sensitivity with computational efficiency. Using coarse-mode data from the 980 observations in dusty days, we derived regional mean values of R_{eff} = 5.24 μm and R_g = 2.43 μm, indicating the predominance of large particles over East Asia. These results are consistent with previous findings for Asian dust transported over South Korea and the Pacific, which typically exhibit modal diameters in the 2–5 μm range (Jeong 2020; Serno et al. 2014; Zdanowicz et al. 2006). A dynamic range of effective radii (1–10 μm) was originally assumed in the operational LUT, representing multiple monomodal lognormal distributions used to compute the dust optical properties. These were then used in radiative transfer simulations to build the LUT relating brightness temperature (BT) to dust AOD. However, this study suggests a more representative range (0.5–5.5 μm) based on observed coarse-mode size distributions for Asian dust in future studies.

4.4 Case Study: Dust Transport Over the Korean Peninsula (March 28-30, 2021 and May 6, 2021)

Two major dust events in spring 2021 were selected based on KMA-reported dusty days: March 28 and May 6. On March 28, East Asia experienced its second severe dust storm of the year, driven results from the updated and operational algorithms by intensified Mongolian cyclones that reduced horizontal visibility to <500 m and generated high winds and convective activity. The dust plume extended over North/Northeast China, the Bohai Sea, and Yellow Sea, with downstream transport to Korea and Japan on March 29–30. More than 60 cities reported elevated PM_{10} concentrations (He et al. 2022).

The May 6 event was triggered by a strong low-pressure system and cold winds over Mongolia. Sea Surface Temperature anomalies in the North Atlantic and eastern Pacific likely intensified the meridional pressure gradient, enhancing surface winds over the Gobi

Desert (Liu et al. 2024). The system produced DAOD values exceeding 1.0 and reduced visibility to < 1 km in parts of China (Yu et al. 2023). These events provide strong meteorological contrast and high dust loading, underscoring their relevance for evaluating retrieval performance.

4.5 Qualitative Validation

To visually assess the spatial and temporal patterns of retrieved dust events, we used RGB composite imagery (Banks et al. 2019) from GK-2 A and DAOD at 10 µm data from IASI-LMD as reference sources. Additionally, true-color imagery helped identify cloud patterns and dust source regions, with similar aerosol distributions observed between the model and reference data. Supplementary Figures S2 and S3 illustrate visual comparisons between True-RGB, false-color RGB, and Up-UM outputs for key time steps on March 28 and May 6, 2021.

For thermal infrared validation, we used IASI-LMD DAOD at 10 µm, one of the few official DAOD products in the TIR spectrum. Although retrieved via a LUT-based method and previously validated (Li et al. 2024), IASI's relatively long revisit time (1 overpass per daytime at 09:30 LST) limits its use for quantitative evaluation.

As shown in Fig. 7, comparisons with DAOD at 11 µm($DAOD_{11\mu m}$) from the Up-UM method reveal broad agreement but also regional discrepancies. Several IASI-detected dust features were not fully captured by the updated method, likely due to differences in temporal coverage, cloud screening criteria, and spectral band differences (10 µm vs. 11 µm). IASI's retrieval omits pixels with cloud or mixed-aerosol influence, focusing only on strong dust signals (Zheng et al. 2023). Despite these differences, Up-UM demonstrates higher spatiotemporal consistency, supported by GK-2 A's continuous monitoring capability. Overall, qualitative validation supports the reliability of the updated method, while also highlighting areas for further refinement.

4.6 Quantitative Validation

We used MODIS onboard Terra satellite for quantitative and qualitative validation in the visible range. The Terra satellite has an equatorial crossing at 10:30 LST over the Korean Peninsula. We projected the MODIS and GK-2 A outputs onto the same maps for a qualitative comparison (Fig. 8).

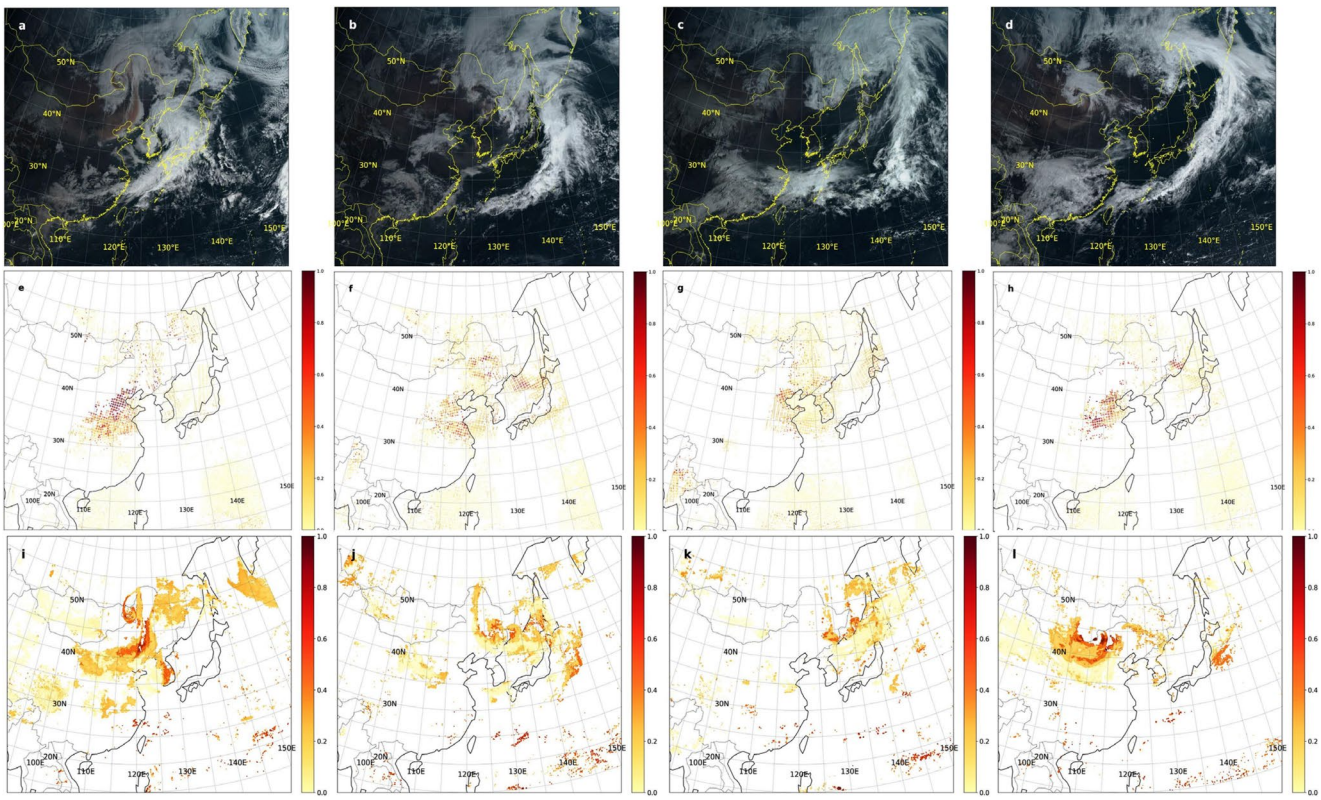

Fig. 7 Panels show (**a–d**) RGB images from the GK-2 A satellite, (**e–h**) DAOD derived from IASI at 10 µm, and (**i–l**) DAOD derived from the Updated-UM algorithm at 11 µm for selected dates. Panels (a, e, i) correspond to March 28, 2021; (b, f, j) to March 29, 2021; (c, g, k) to March 30, 2021; and (d, h, l) to May 6, 2021. The MetOp-A satellite overpass time for IASI in the descending (daytime) pass is approximately 00:30 UTC (09:30 local time). This layout illustrates spatial and temporal similarities and differences between the two retrieval methods and the satellite observations

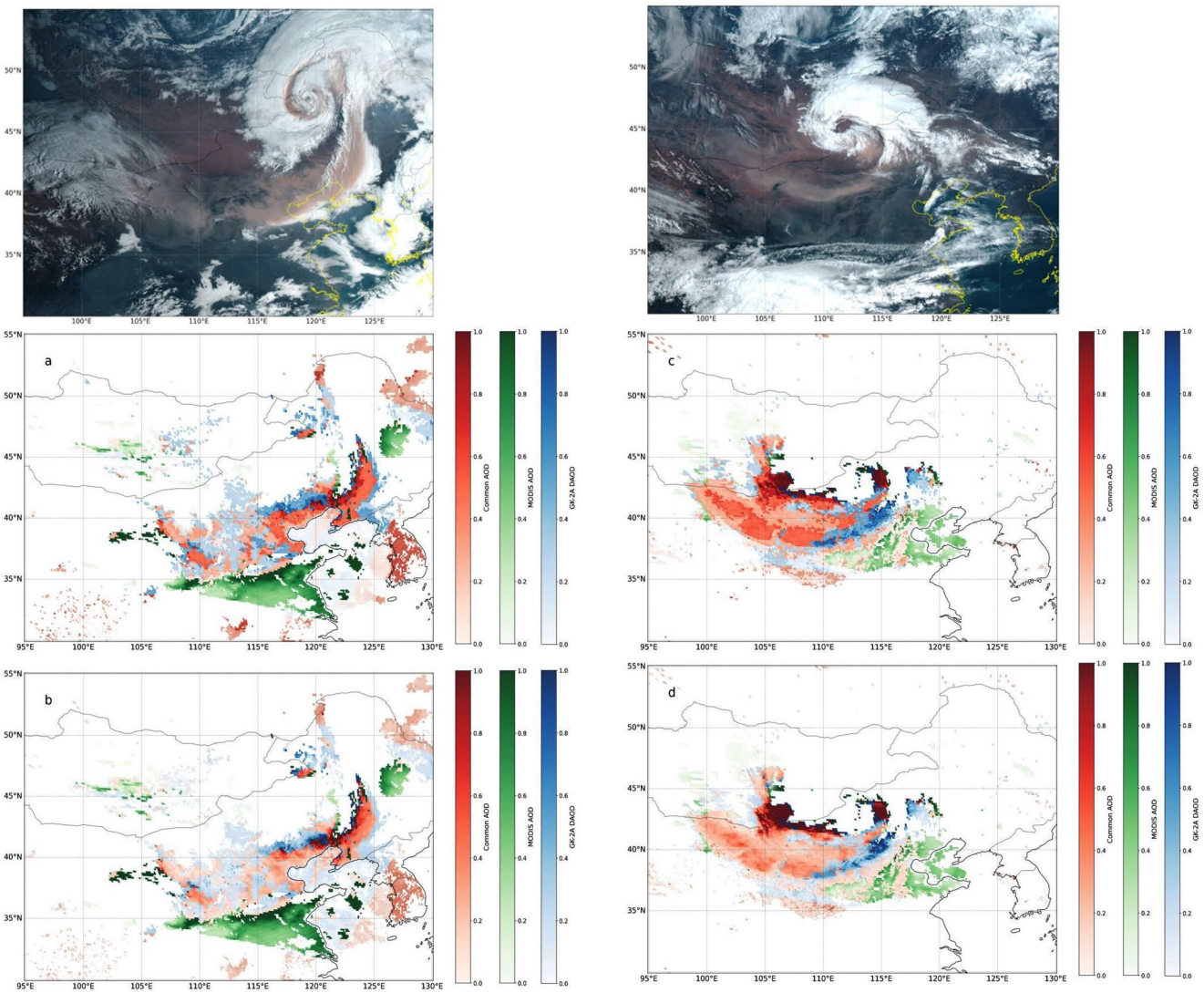

Fig. 8 Composite comparison of GK-2 A RGB imagery and dust detection results from the updated and operational algorithms, along with MODIS AOD (550 nm), for two major dust events. Top row: True-color RGB images from GK-2 A for (left) March 28, 2021, at 03:25 UTC, and (right) May 6, 2021, at 03:30 UTC. Middle and bottom rows: Spatial dust detection maps at 11 μm comparing MODIS and GK-2 A retrievals. Panels (**a**, **b**) correspond to March 28: (a) updated algorithm (Up–UM); (b) operational algorithm (Op–UM). Panels (**c**, **d**) correspond to May 6: (c) updated; (d) operational. Red: dust detected by both GK-2 A and MODIS; Green: MODIS only; Blue: GK-2 A only

It is crucial to note that the MODIS products illustrate total AOD, whereas the updated method outputs focus only on dust AOD. The mismatch observed in eastern China was significant in both case studies, likely due to the high concentrations of anthropogenic aerosols, especially black carbon, which are fine-mode particles with strong absorption characteristics (Park et al. 2014). In the first case study (March 28, 2021), the discontinuity between land and sea in the GK-2A TIR-based dust detection results were noticeable. This may be attributed to the influence of background brightness temperature assumptions and surface emissivity contrasts across land-ocean boundaries, which affect the performance of the dust detection algorithm. Moreover, the updated algorithm outputs shown in Fig. 8 (a and c) yield higher AOD values compared to the operational algorithm outputs (b and d), which can be attributed to the stronger absorption characteristics of the refractive index, leading to higher attenuation of light. For quantitative comparison, overlapping pixels of MODIS and GK-2A were divided into 0.25° × 0.25° to obtain finer details and improve accuracy by minimizing the averaging effect. The comparison of six methods (Up-UM, Up-AD, Up-Fix, Op-UM, Op-AD, and Op-Fix) against MODIS 550 nm AOD data for May 6, 2021 is illustrated in Fig. 9. Results for other dates are summarized in Table 6, along with three evaluation metrics including correlation (R^2), slope (b), and mean bias error (MBE) (Fig. 10).

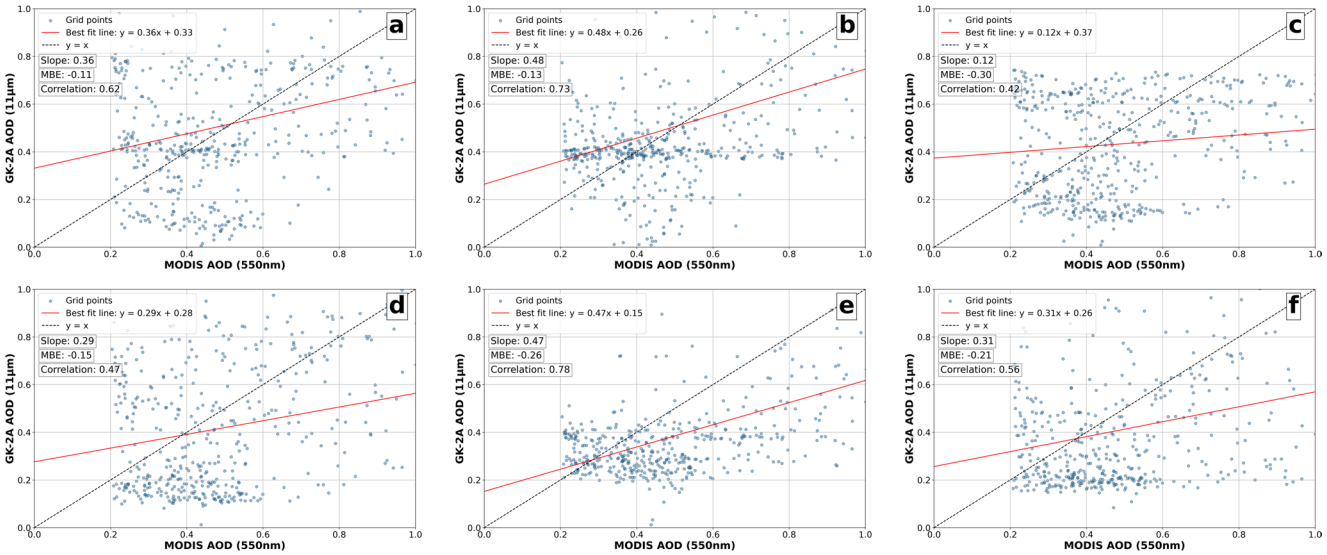

Fig. 9 Scatter plots comparing DAOD at 11 μm with MODIS AOD at 550 nm on May 6, 2021 for (a) Up-UM, (b) Up-AD, (c) Up-Fix, (d) Op-UM, (e) Op-AD, and (f) Op-Fix methods

Table 6 Evaluation of the performances of six dust retrieval algorithms in this study at 11 μm compared to MODIS 550 nm AOD in case studies, using statistical metrics (Correlation (R^2), slope (b), and mean bias error (MBE))

Date	Metrics	Up-UM	Up-AD	Up-Fix	Op-UM	Op-AD	Op-Fix
March 28, 2021	R^2	0.77	0.72	0.35	0.56	0.71	0.86
	Slope	0.63	0.34	0.17	0.41	0.25	0.67
	MBE	−0.12	−0.29	−0.32	−0.16	−0.30	−0.24
March 29, 2021	R^2	0.60	0.60	0.56	0.56	0.55	0.47
	Slope	0.56	0.46	0.34	0.39	0.47	0.18
	MBE	−0.17	−0.24	−0.30	−0.23	−0.23	−0.28
March 30, 2021	R^2	0.40	0.38	0.11	0.45	0.22	0.41
	Slope	0.37	0.42	0.10	0.39	0.16	0.14
	MBE	−0.16	−0.24	−0.08	−0.31	−0.45	−0.46
May 6, 2021	R^2	0.62	0.73	0.42	0.47	0.78	0.56
	Slope	0.36	0.48	0.12	0.29	0.47	0.31
	MBE	−0.11	0.−13	−0.30	−0.15	−0.26	−0.21

The metrics showed significant variability among the retrieval algorithms and dates. On March 28, 2021, the performance of all algorithms indicated high agreement with the observed data (MODIS), except for the Up-Fix (0.35) and Op-UM (0.56) methods. As discussed earlier, East Asia experienced the second most severe dust outbreak on this date. Due to increased dust loading, the high AOD during this event likely provided strong signals, which enabled the algorithms to capture them easily and significantly improve the correlation; this is particularly true for algorithms such as Op-Fix (0.86) and Up-UM (0.77), which exhibited excellent performance. However, unacceptable performances on March 30, 2021 reflect serious challenges for detecting and retrieving dust properties under less severe conditions for all algorithms. Overall, update-based algorithms show better correlations than operational algorithms in most cases, indicating a general improvement in the predictive ability of the methods. These improvements were evident in Up-UM and Up-AD, where the R^2 values were consistently higher than their operational counterparts. However, the Up-Fix method that relies on fixed DLH is neither scientific nor practical. These results for a fixed DLH were anticipated, as a fixed height hinders the capture of the variability introduced by factors such as topography and natural dynamics in the vertical distribution of dust. Surprisingly, similar trends were not observed with the Op-Fix method, and the reason for this remains unclear. Further studies are required to provide further insights into these results.

Across all algorithms, MBE consistency had negative quantities, reflecting a tendency for the underestimation of GK-2 A dust AOD compared to MODIS total AOD values. The Up-UM algorithm had the lowest MBE in most cases, specifically on March 28, 2021, indicating more accuracy in retrievals regarding overall bias than other algorithms. In

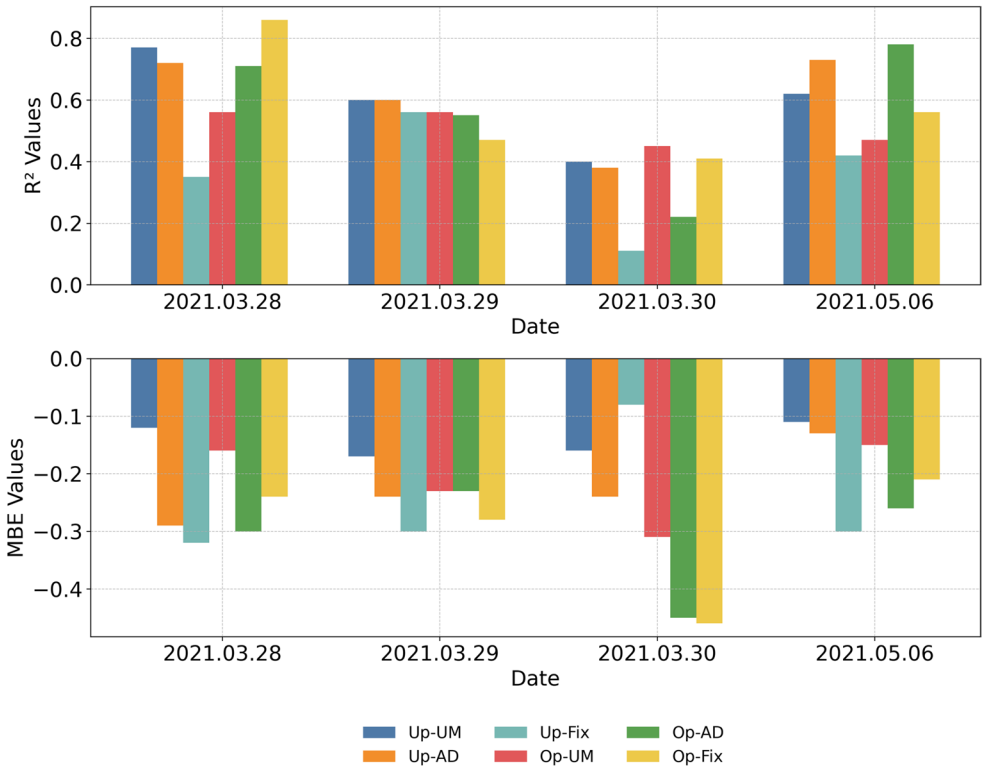

Fig. 10 Comparison of six dust retrieval methods (Up-UM, Up-AD, Up-Fix, Op-UM, Op-AD, Op-Fix) at 11 μm against MODIS 550 nm AOD data across different dates (March 28, March 29, March 30, and May 6, 2021) using correlation (R^2) and mean bias error (MBE) to access the performance of each method in estimating the DAOD

contrast, Up-Fix regularly shows larger biases as anticipated, emphasizing that DLH creates serious discrepancies and inconsistencies as a fixed layer through transport. Among the algorithms, the operational ones tended to have slightly higher negative MBE values, indicating a higher underestimation of AOD. Generally, the results indicate that all algorithms exhibit some biases; however, Up-UM appears to be the least biased (Fig. 11).

Peyridieu et al. (2013) defined an acceptable experimental ratio for $DAOD_{TIR}/AOD_{VIS}$ within the range of 28–65% (Zheng et al. 2023). This range suggests that the DAOD in the TIR region is expected to contribute approximately 28–65% of the total AOD measured in the visible regions. On March 28, the Up-UM algorithm showed strong agreement (63%) between the predicted and observed data. However, Up-AD and Up-Fix methods show Limitations according to weaker alignment with slopes of 0.34 and 0.17, respectively. Although the Op-Fix method outperformed the Up-UM algorithm on this specific date, the weak performance of this algorithm on other dates indicated that this method was unreliable across various conditions. On March 29, all slopes were under 0.6, with Up-UM (56%)

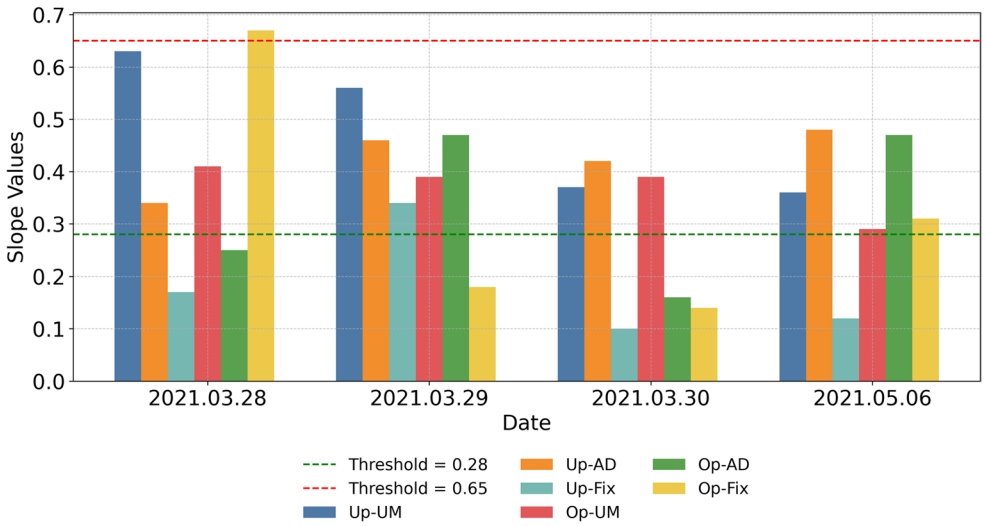

Fig. 11 Comparison of slope (b) of the best-fit line between six dust retrieval methods (Up-UM, Up-AD, Up-Fix, Op-UM, Op-AD, Op-Fix) against MODIS 550 nm AOD data across different dates. The minimum and maximum threshold is based on the experimental ratio for $DAOD_{TIR}/AOD_{vis,}$ with an acceptable range between 0.28 and 0.65 (Peyridieu et al. 2013)

showing a slightly better performance than the others. Conversely, on May 6, the Up-AD and Op-UM algorithms outweigh the other methods and demonstrate stronger predictive performance for this event. Overall, several algorithms, including Up-UM, Op-UM, and Up-AD, fell within the allowed range; specifically, Up-AD and Op-UM showed more consistency and lower variances. The fixed DLH (Up-Fix and Op-Fix) algorithms show values below or above the allowed range, and the performance of the Op-AD method is unreliable.

5 Conclusions and Perspectives

In this study, we calculated a refractive index specifically designed for Asian dust based on observational chemical composition data collected in South Korea during long-term dust events. The obtained refractive index was then compared with highly cited refractive index datasets to illustrate the differences and similarities. Our results show that the real part of the refractive index in Asian dust has a similar trend to that of other datasets with different Magnitudes. In contrast, the imaginary part was completely different in shape and Magnitude, reflecting the diversity of dust sources. The imaginary part is notably higher in the region between 8 and 10 μm, where the absorption of quartz (9.2 μm) and clay minerals (9.6 μm) is maximum. This peak is likely attributable to the large proportion of clay minerals and Quartz in Asian dust (48% and 20%, respectively).

Additionally, the impact of DLH using the UM and ADAM3 numerical weather prediction models and the fixed layer height method was investigated. To this end, we designed an algorithm (Updated) similar to the currently operational algorithm, with specific modifications related to the Asian refractive index and the three DLH determination methods. For the sensitivity tests, the results of the Updated algorithms with those of the GK-2 A operational algorithm were compared. To remove the effects of other variables on the sensitivity tests, we maintained the assumptions and dust detection method similar to those of the operational algorithm.

We compared the results with GK-2 A RGB-true color, RGB-dust products, and IASI-LMD 10 μm AOD for qualitative validation. For quantitative validation, MODIS 550 nm AOD was applied. Visible-based validation has two main considerations. First, owing to differences in tools, spectral ranges, and algorithms, comparisons between the TIR and visible regions inherently cause discrepancies. Second, visible-based validation was chosen due to limited availability of officially released, validated, and reliable references in the TIR region. Surprisingly, although qualitative comparisons with GK-2 A RGB products and IASI-LMD data showed satisfactory results in specific areas, considerable mismatches were also observed in several regions. These misalignments can be attributed to the dust detection algorithm used in the current operational algorithm, which must be addressed in future studies.

According to a quantitative comparison with MODIS validations conducted for case studies on March 28 and May 6, 2021, the performance of the updated-based algorithms, except for the Up-Fix method, outweighs the operational methods. The Up-UM method exhibited the highest correlations and lowest mean bias errors in most cases. As expected, the Fixed DLH obtained using the updated algorithm failed to capture the variability in the vertical distribution of dust particles, resulting in low and inconsistent correlations and a large MBE. Interestingly, the Op-Fix algorithm showed completely inverted results. The reasons for this remain unclear and should be investigated in future studies. These findings highlight the importance of accuracy in DLH determination, especially in thermal infrared regions, to improve the reliability and precision of algorithms.

This study presents a refractive index tailored for Asian dust, derived from observational chemical composition data, offering an alternative to commonly used assumptions or theoretically optimized values. By using region-specific inputs, the proposed dataset aims to reduce potential biases introduced by applying refractive indices derived from non-Asian dust sources in East Asian modeling and remote sensing applications.

Despite the valuable insights this study provides, several limitations must be noted. One of the most significant limitations is the limited number of case studies, primarily due to the unavailability of the ADAM3 models, which considerably reduced the number of analyzed cases. To address this issue, we evaluated our results using various validation sources with the highest accuracy, including visible and TIR-based sources. Another limitation arises from simplified assumptions that do not fully reflect real-world conditions—such as assuming spherical dust particles, fixed size distributions, and background brightness temperature handling. These assumptions were applied to ensure consistent conditions for sensitivity tests and to minimize confounding effects when comparing accuracy with the operational algorithms. In future studies, we will modify these assumptions to increase the applicability of the findings to specific algorithms designed for dust retrieval in thermal infrared. Finally, dust detection and retrieval were conducted only during the day, owing to limitations in the availability of validation sources during the night. We plan to expand the validations to night-time using active satellite sensors such as Cloud-Aerosol Lidar with Orthogonal Polarization and moon photometer data from AERONET.

Supplementary Information The online version contains supplementary material available at https://doi.org/10.1007/s13143-025-00410-x.

Acknowledgements This work was supported by the Meteorological Administration Research and Development Program under Grant RS-2024-00404042.

Funding Open Access funding enabled and organized by Ulsan National Institute of Science and Technology (UNIST).

Declarations

Conflict of interest The authors declare that they have no conflict of interest.

References

Ackerman, S.A.: Remote sensing aerosols using satellite infrared observations. Journal of Geophysical Research: Atmospheres **102**, 17069–17079 (1997). https://doi.org/10.1029/96jd03066

Adebiyi, A.A., Kok, J.F.: Climate models miss most of the coarse dust in the atmosphere. Sci. Adv. **6**, eaaz9507 (2020). https://doi.org/10.1126/sciadv.aaz9507

Adebiyi, A.A., Kok, J.F.: Climate models miss most of the coarse dust in the atmosphere. Sci. Adv. **6**, eaaz9507 (2024). https://doi.org/10.1126/sciadv.aaz9507

Ahn, S., Kim, H.S., Byon, J.Y., Lim, H.: Improving dust aerosol optical depth (DAOD) retrieval from the GEOKOMPSAT-2A (GK-2A) satellite for daytime and nighttime monitoring. Remote Sens. (Basel). **24**, 1490 (2024). https://doi.org/10.3390/s24051490

Alalam, P., Ducos, F., Herbin, H.: The role of refractive indices in measuring mineral dust with high-spectral resolution infrared satellite sounders: Application to the gobi desert. Atmos. Chem. Phys. **24**, 12277–12294 (2024). https://doi.org/10.5194/egusphere-2024-888

Amgalan, G., Liu, G.R., Lin, T.H., Kuo, T.H.: Correlation between dust events in Mongolia and surface wind and precipitation. Terr. Atmos. Ocean. Sci. **28**, 23–32 (2017). https://doi.org/10.3319/Tao.2016.04.25.01(Cca)

Arnold, J.A., Glotch, T.D., Plonka, A.M.: Mid-infrared optical constants of clinopyroxene and orthoclase derived from oriented single-crystal reflectance spectra. Am. Mineral. **99**, 1942–1955 (2014). https://doi.org/10.2138/am-2014-4828

Baddock, M.C., Strong, C.L., Leys, J.F., Heidenreich, S.K., Tews, E.K., McTainsh, G.H.: A visibility and total suspended dust relationship. Atmos. Environ. **89**, 329–336 (2014). https://doi.org/10.1016/j.atmosenv.2014.02.038

Baldo, C., Formenti, P., Nowak, S., Chevaillier, S., Cazaunau, M., Pangui, E., Di Biagio, C., Doussin, J.F., Ignatyev, K., Dagsson-Waldhauserova, P., Arnalds, O., MacKenzie, A.R., Shi, Z.B.: Distinct chemical and mineralogical composition of Icelandic dust compared to Northern African and Asian dust. Atmos. Chem. Phys. **20**, 13521–13539 (2020). https://doi.org/10.5194/acp-20-13521-2020

Banks, J.R., Hünerbein, A., Heinold, B., Brindley, H.E., Deneke, H., Schepanski, K.: The sensitivity of the colour of dust in MSG-SEVIRI desert dust infrared composite imagery to surface and atmospheric conditions. Atmos. Chem. Phys. **19**, 6893–6911 (2019). https://doi.org/10.5194/acp-19-6893-2019

Bhatia, M.R., Crook, K.A.W.: Trace-Element characteristics of graywackes and tectonic setting discrimination of sedimentary basins. Contrib. Mineral. Petrol. **92**, 181–193 (1986). https://doi.org/10.1007/Bf00375292

Bi, L., Ding, S.G., Zong, R.R., Yi, B.Q.: Examining Asian dust refractive indices for brightness temperature simulations in the 650–1135 cm−1 spectral range. Journal of Quantitative Spectroscopy and Radiative Transfer **247**, 106945 (2020). https://doi.org/10.1016/j.jqsrt.2020.106945

Bilal, M., Nichol, J.E., Wang, L.C.: New customized methods for improvement of the MODIS C6 dark target and deep blue merged aerosol product. Remote Sens. Environ. **197**, 115–124 (2017). https://doi.org/10.1016/j.rse.2017.05.028

Bruggeman, D.A.G.: Berechnung verschiedener physikalischer Konstanten von heterogenen substanzen. I. Dielektrizitätskonstanten und leitfähigkeiten der Mischkörper Aus isotropen substanzen. Annalen der Physik **416**, 636–664 (1935). https://doi.org/10.1002/andp.19354160705

Callewaert, S., Vandenbussche, S., Kumps, N., Kylling, A., Shang, X.X., Komppula, M., Goloub, P., De Mazière, M.: The mineral aerosol profiling from infrared radiances (MAPIR) algorithm: Version 4.1 description and evaluation. Atmos. Meas. Tech. **12**, 3673–3698 (2019). https://doi.org/10.5194/amt-12-3673-2019

Capelle, V., Chédin, A., Siméon, M., Tsamalis, C., Pierangelo, C., Pondrom, M., Crevoisier, C., Crepeau, L., Scott, N.A.: Evaluation of IASI-derived dust aerosol characteristics over the tropical belt. Atmos. Chem. Phys. **14**, 9343–9362 (2014). https://doi.org/10.5194/acp-14-9343-2014

Castellanos, P., Colarco, P., Espinosa, W.R., Guzewich, S.D., Levy, R.C., Miller, R.L., Chin, M., Kahn, R.A., Kemppinen, O., Moosmüller, H., Nowottnick, E.P., Rocha-Lima, A., Smith, M.D., Yorks, J.E., Yu, H.B.: Mineral dust optical properties for remote sensing and global modeling: A review. Remote Sens. Environ. **303**, 113982 (2024). https://doi.org/10.1016/j.rse.2023.113982

Cavazzani, S., Zitelli, V., Ortolani, S.: Long-term analysis of clear Sky at astronomical sites: A comparison between Polar and geostationary satellites. Mon not R Astron. Soc **452**, 2185–2194 (2015). https://doi.org/10.1093/mnras/stv1319

Chen, B., Zhang, P., Zhang, B.D., Jia, R., Zhang, Z.J., Wang, T.H., Zhou, T.: An overview of passive and active dust detection methods using satellite measurements. J. Meteorol. Res. **28**, 1029–1040 (2014). https://doi.org/10.1007/s13351-014-4032-4

Chen, Q.X., Huang, C.L., Dong, S.K., Lin, K.F.: Satellite-Based background aerosol optical depth determination via global statistical analysis of multiple lognormal distribution. Remote Sens. (Basel). **16**, 1210 (2024). https://doi.org/10.3390/rs16071210

Clarisse, L., Clerbaux, C., Franco, B., Hadji-Lazaro, J., Whitburn, S., Kopp, A.K., Hurtmans, D., Coheur, P.F.: A Decadal Data Set of Global Atmospheric Dust Retrieved From IASI Satellite Measurements. J. Geophys. Res. Atmos. **124**, 1618–1647 (2019). https://doi.org/10.1029/2018jd029701

Dash, P., Göttsche, F.M., Olesen, F.S., Fischer, H.: Land surface temperature and emissivity Estimation from passive sensor data::

Theory and practice-current trends. Int. J. Remote Sens. **23**, 2563–2594 (2002). https://doi.org/10.1080/01431160110115041

De Paepe, B., Dewitte, S.: Dust aerosol optical depth retrieval over a desert surface using the SEVIRI window channels. Journal of Atmospheric and Oceanic Technology **26**, 704–718 (2009). https://doi.org/10.1175/2008jtecha1109.1

Dentener, F.J., Carmichael, G.R., Zhang, Y., Lelieveld, J., Crutzen, P.J.: Role of mineral aerosol as a reactive surface in the global troposphere. Journal of Geophysical Research: Atmospheres **101**, 22869–22889 (1996). https://doi.org/10.1029/96JD01818

DeSouza-Machado, S.G., Strow, L.L., Imbiriba, B., McCann, K., Hoff, R.M., Hannon, S.E., Martins, J.V., Tanré, D., Deuzé, J.L., Ducos, F., Torres, O.: Infrared retrievals of dust using AIRS: Comparisons of optical depths and heights derived for a North African dust storm to other collocated EOS A-Train and surface observations. Journal of Geophysical Research: Atmospheres (D15),(2010). https://doi.org/10.1029/2009jd012842

Di Biagio, C., Formenti, P., Balkanski, Y., Caponi, L., Cazaunau, M., Pangui, E., Journet, E., Nowak, S., Caquineau, S., Andreae, M.O., Kandler, K., Saeed, T., Piketh, S., Seibert, D., Williams, E., Doussin, J.F.: Global scale variability of the mineral dust longwave refractive index: A new dataset of in situ measurements for climate modeling and remote sensing. Atmos. Chem. Phys. **17**, 1901–1929 (2017). https://doi.org/10.5194/acp-17-1901-2017

Dubovik, O., Smirnov, A., Holben, B.N., King, M.D., Kaufman, Y.J., Eck, T.F., Slutsker, I.: Accuracy assessments of aerosol optical properties retrieved from aerosol robotic network (AERONET) sun and Sky radiance measurements. Journal of Geophysical Research: Atmospheres **105**(D8), 9791–9806 (2000). https://doi.org/10.1029/2000jd900040

Dunion, J.P., Velden, C.S.: The impact of the saharan air layer on Atlantic tropical cyclone activity. Bulletin of the American Meteorological Society **85**, 353–366 (2004). https://doi.org/10.1175/Bams-85-3-353

Eom, S., Kim, J., Lee, S.Y., Holben, B.N., Eck, T.F., Park, S.B., Park, S.S.: Long-term variation of aerosol optical properties associated with aerosol types over East Asia using AERONET and satellite (VIIRS, OMI) data (2012–2019). Atmospheric Research **280**, 106457 (2022). https://doi.org/10.1016/j.atmosres.2022.106457

Fraser, R.S., Kaufman, Y.J.: The relative importance of aerosol scattering and absorption in Remote-Sensing. IEEE Trans. Geosci. Remote Sens. GE. **–23**, 625–633 (1985). https://doi.org/10.1109/Tgrs.1985.289380

Froyd, K.D., Yu, P.F., Schill, G.P., Brock, C.A., Kupc, A., Williamson, C.J., Jensen, E.J., Ray, E., Rosenlof, K.H., Bian, H.S., Darmenov, A.S., Colarco, P.R., Diskin, G.S., Bui, T., Murphy, D.M.: Dominant role of mineral dust in cirrus cloud formation revealed by global-scale measurements. Nat. Geosci. **15**, 177–183 (2022). https://doi.org/10.1038/s41561-022-00901-w

Garnett, J.C.M., Larmor, J.: XII. Colours in metal glasses and in metallic films. Philos. Trans. R Soc. Lond. A. **203**, 385–420 (1997). https://doi.org/10.1098/rsta.1904.0024

Georgoulias, A.K., Alexandri, G., Kourtidis, K.A., Lelieveld, J., Zanis, P., Pöschl, U., Levy, R., Amiridis, V., Marinou, E., Tsikerdekis, A.: Spatiotemporal variability and contribution of different aerosol types to the aerosol optical depth over the Eastern mediterranean. Atmos. Chem. Phys. **16**, 13853–13884 (2016). https://doi.org/10.5194/acp-16-13853-2016

Hamilton, D.S., Baker, A.R., Iwamoto, Y., Gasso, S., Bergas-Masso, E., Deutch, S., Dinasquet, J., Kondo, Y., Llort, J., Myriokefalitakis, S., Perron, M.M.G., Wegmann, A., Yoon, J.E.: An aerosol odyssey: Navigating nutrient flux changes to marine ecosystems. Elem. Sci. Anth. (2023). https://doi.org/10.1525/elementa.2023.00037

He, T., Liu, L.W., Chen, Y., Sheng, X.F., Ji, J.F.: Plagioclase subspecies in Chinese loess deposits: Implications for dust source migration and past climate change. Quat Res **85**, 17–24 (2016). https://doi.org/10.1016/j.yqres.2015.12.004

He, Y., Yi, F., Yin, Z.P., Liu, F.C., Yi, Y., Zhou, J.: Mega Asian dust event over China on 27–31 March 2021 observed with spaceborne instruments and ground-based polarization lidar. Atmos. Environ. **285**, 119238 (2022). https://doi.org/10.1016/j.atmosenv.2022.119238

Hess, M., Koepke, P., Schult, I.: Optical properties of aerosols and clouds: The software package OPAC. Bulletin of the American Meteorological Society **79**, 831–844 (1998)

Highwood, E.J., Haywood, J.M., Silverstone, M.D., Newman, S.M., Taylor, J.P.: Radiative properties and direct effect of saharan dust measured by the C-130 aircraft during saharan dust experiment (SHADE): 2. Terrestrial spectrum. J. Geophys. Res. Atmos. **108**, 6 (2003). https://doi.org/10.1029/2002jd002552

Holben, B.N., Eck, T.F., Slutsker, I., Tanre, D., Buis, J.P., Setzer, A., Vermote, E., Reagan, J.A., Kaufman, Y.J., Nakajima, T., Lavenu, F., Jankowiak, I., Smirnov, A.: AERONET - A federated instrument network and data archive for aerosol characterization. Remote Sensing of Environment **66**, 1–16 (1998). https://doi.org/10.1016/S0034-4257(98)00031-5

Hsu, N.C., Jeong, M.J., Bettenhausen, C., Sayer, A.M., Hansell, R., Seftor, C.S., Huang, J., Tsay, S.C.: Enhanced deep blue aerosol retrieval algorithm: The second generation. J. Geophys. Res. Atmos. **118**, 9296–9315 (2013). https://doi.org/10.1002/jgrd.50712

Jang, J.C., Lee, S., Sohn, E.H., Noh, Y.J., Miller, S.D.: Combined dust detection algorithm for Asian dust events over East Asia using GK2A/AMI: A case study in October 2019. Asia-Pacific Journal of Atmospheric Sciences **58**, 45–64 (2022). https://doi.org/10.1007/s13143-021-00234-5

Jeong, G.Y.: Bulk and single-particle mineralogy of Asian dust and a comparison with its source soils. Journal of Geophysical Research: Atmospheres **113**, Article 2 (2008). https://doi.org/10.1029/2007jd008606

Jeong, G.Y.: Mineralogy and geochemistry of Asian dust: Dependence on migration path, fractionation, and reactions with polluted air. Atmos. Chem. Phys. **20**, 7411–7428 (2020). https://doi.org/10.5194/acp-20-7411-2020

Jeong, G.Y., Nousiainen, T.: TEM analysis of the internal structures and mineralogy of Asian dust particles and the implications for optical modeling. Atmos. Chem. Phys. **14**, 7233–7254 (2014). https://doi.org/10.5194/acp-14-7233-2014

Jeong, G.Y., Kim, J.Y., Seo, J., Kim, G.M., Jin, H.C., Chun, Y.: Long-range transport of giant particles in Asian dust identified by physical, mineralogical, and meteorological analysis. Atmos. Chem. Phys. **14**, 505–521 (2014). https://doi.org/10.5194/acp-14-505-2014

Jeong, G.Y., Park, M.Y., Kandler, K., Nousiainen, T., Kemppinen, O.: Mineralogical properties and internal structures of individual fine particles of saharan dust. Atmos. Chem. Phys. **16**, 12397–12410 (2016). https://doi.org/10.5194/acp-16-12397-2016

Ji, W.Q., Yang, L.K., Tian, X.Y., Bilal, M., Pei, X., Zheng, Y., Lu, X.F., Cheng, X.Q.: Long-term validation and error analysis of DB and MAIAC aerosol products over bright surface of China. Atmospheric Research **297**, 107106 (2024). https://doi.org/10.1016/j.atmosres.2023.107106

Johnson, M.S., Meskhidze, N.: Atmospheric dissolved iron deposition to the global oceans: Effects of oxalate-promoted Fe dissolution, photochemical redox cycling, and dust mineralogy. Geosci. Model. Dev. **6**, 1137–1155 (2013). https://doi.org/10.5194/gmd-6-1137-2013

Kam, Z.: Absorption and scattering of light by small Particles - Bohren,C, huffman,dr. Nature. **306**, 625 (1983). https://doi.org/10.1038/306625a0

Kanayama, S., Yabuki, S., Yanagisawa, F., Motoyama, R.: The chemical and strontium isotope composition of atmospheric aerosols over japan: The contribution of long-range-transported Asian dust

(Kosa). Atmos. Environ. **36**, 5159–5175 (2002). https://doi.org/10.1016/S1352-2310(02)00587-3

Kandler, K., Lieke, K., Benker, N., Emmel, C., Küpper, M., Müller-Ebert, D., Ebert, M., Scheuvens, D., Schladitz, A., Schütz, L., Weinbruch, S.: Electron microscopy of Particles collected at praia, cape verde, during the saharan mineral dust experiment: Particle chemistry, shape, mixing state and complex refractive index. Tellus B Chem. Phys. Meteorol. **63**, 475–496 (2011). https://doi.org/10.1111/j.1600-0889.2011.00550.x

Kawai, K., Matsui, H., Tobo, Y.: Dominant role of Arctic dust with high ice nucleating ability in the Arctic lower troposphere. Geophys. Res. Lett. **50**, e2022GL102470 (2023). https://doi.org/10.1029/2022GL102470

Kim, D., Chin, M., Schuster, G., Yu, H.B., Takemura, T., Tuccella, P., Ginoux, P., Liu, X.H., Shi, Y., Matsui, H., Tsigaridis, K., Bauer, S.E., Kok, J.F., Schulz, M.: Where Dust Comes From: Global Assessment of Dust Source Attributions With AeroCom Models. Journal of Geophysical Research: Atmospheres **129**, eJD041377 (2024). https://doi.org/10.1029/2024JD041377

Kitamura, R., Pilon, L., Jonasz, M.: Optical constants of silica glass from extreme ultraviolet to Far infrared at near room temperature. Appl. Opt. **46**, 8118–8133 (2007). https://doi.org/10.1364/Ao.46.008118

Klüser, L., Martynenko, D., Holzer-Popp, T.: Thermal infrared remote sensing of mineral dust over land and ocean: A spectral SVD based retrieval approach for IASI. Atmos. Meas. Tech. **4**, 757–773 (2011). https://doi.org/10.5194/amt-4-757-2011

Kok, J.F., Adebiyi, A.A., Albani, S., Balkanski, Y., Checa-Garcia, R., Chin, M., Colarco, P.R., Hamilton, D.S., Huang, Y., Ito, A., Klose, M., Li, L., Mahowald, N.M., Miller, R.L., Obiso, V., García-Pando, P., Rocha-Lima, C., Wan, A.: Contribution of the world's main dust source regions to the global cycle of desert dust. Atmos. Chem. Phys. **21**, 8169–8193 (2021). https://doi.org/10.5194/acp-21-8169-2021

Kong, S.Y., Wang, Z., Bi, L.: Uncertainties in laboratory-measured shortwave refractive indices of mineral dust aerosols and derived optical properties: A theoretical assessment. Atmos. Chem. Phys. **24**, 6911–6935 (2024). https://doi.org/10.5194/acp-24-6911-2024

Kylling, A., Vandenbussche, S., Capelle, V., Cuesta, J., Klüser, L., Lelli, L., Popp, T., Stebel, K., Veefkind, P.: Comparison of dust-layer heights from active and passive satellite sensors. Atmos. Meas. Tech. **11**, 2911–2936 (2018). https://doi.org/10.5194/amt-11-2911-2018

L'Ecuyer, T.S., Jiang, J.H.: Touring the atmosphere aboard the A-Train. Phys. Today **63**, 36–41 (2010). https://doi.org/10.1063/1.3463626

Lee, K.-M., Park, J.-H.: Optical constants for Asian dust in midinfrared region. Journal of Geophysical Research: Atmospheres **119**, 927–942 (2014). https://doi.org/10.1002/2013JD020207

Lee, E.H., Sohn, B.J.: Recent increasing trend in dust frequency over Mongolia and inner Mongolia regions and its association with climate and surface condition change. Atmos. Environ. **45**, 4611–4616 (2011). https://doi.org/10.1016/j.atmosenv.2011.05.065

Lee, H.J., Liu, Y., Coull, B.A., Schwartz, J., Koutrakis, P.: A novel calibration approach of MODIS AOD data to predict PM concentrations. Atmos. Chem. Phys. **11**, 7991–8002 (2011). https://doi.org/10.5194/acp-11-7991-2011

Lee, J., Hsu, N.C., Bettenhausen, C., Sayer, A.M., Seftor, C.J., Jeong, M.J.: Retrieving the height of smoke and dust aerosols by synergistic use of VIIRS, OMPS, and CALIOP observations. Journal of Geophysical Research: Atmospheres **120**, 8372–8388 (2015). https://doi.org/10.1002/2015jd023567

Leinen, M., Prospero, J.M., Arnold, E., Blank, M.: Mineralogy of aeolian dust reaching the North Pacific-Ocean.1. Sampling and analysis. J. Geophys. Res. Atmos. **99**, 21017–21023 (1994). https://doi.org/10.1029/94jd01735

Letu, H., Shi, J.C., Li, M., Wang, T.X., Shang, H.Z., Lei, Y.H., Ji, D.B., Wen, J.G., Yang, K., Chen, L.F.: A review of the Estimation of downward surface shortwave radiation based on satellite data: Methods, progress and problems. Sci. China Earth Sci. **63**, 774–789 (2020). https://doi.org/10.1007/s11430-019-9589-0

Li, Z.L., Li, J., Li, Y., Zhang, Y., Schmit, T.J., Zhou, L.H., Goldberg, M.D., Menzel, W.P.: Determining diurnal variations of land surface emissivity from geostationary satellites. Journal of Geophysical Research: Atmospheres (D23),(2012). https://doi.org/10.1029/2012jd018279

Li, J., Wong, M.S., Shi, G.Q., Nichol, J.E., Lee, K.H., Chan, P.: Advanced algorithms on monitoring diurnal variations in dust aerosol properties using geostationary satellite imagery. Remote Sens. Environ. **303**, 113996 (2024). https://doi.org/10.1016/j.rse.2024.113996

Liu, Y., Liu, R.G., Cheng, X.: Dust detection over desert surfaces with thermal infrared bands using dynamic reference brightness temperature differences. Journal of Geophysical Research: Atmospheres **118**, 8566–8584 (2013). https://doi.org/10.1002/jgrd.50647

Liu, L., Wang, Z.L., Che, H.Z., Wang, D.Y., Gui, K., Liu, B., Ma, K.J., Zhang, X.Y.: Climate factors influencing springtime dust activities over Northern East Asia in 2021 and 2023. Atmospheric Research **303**, 107342 (2024). https://doi.org/10.1016/j.atmosres.2024.107342

Ma, Y.Y., Gong, W., Wang, P.C., Hu, X.Q.: New dust aerosol identification method for spaceborne lidar measurements. Journal of Quantitative Spectroscopy and Radiative Transfer **112**, 338–345 (2011). https://doi.org/10.1016/j.jqsrt.2010.08.004

Macdonald, M., Anderson, P., Carrea, L., Dobke, B., Embury, O., Merchant, C., Bensi, P.: Concepts for a geostationary-like Polar mission. Proc. SPIE Int. Soc. Opt. Eng. **9241**, 328–343 (2014). https://doi.org/10.1117/12.2067142

Masuda, K., Mano, Y., Ishimoto, H., Tokuno, M., Yoshizaki, Y., Okawara, N.: Assessment of the nonsphericity of mineral dust from geostationary satellite measurements. Remote Sens. Environ. **82**, 238–247 (2002). https://doi.org/10.1016/S0034-4257(02)00040-8

Mayer, B., Kylling, A.: Technical note: The libradtran software package for radiative transfer calculations - description and examples of use. Atmos. Chem. Phys. **5**, 1855–1877 (2005). https://doi.org/10.5194/acp-5-1855-2005

Mooney, T., Knacke, R.F.: Optical-Constants of chlorite and serpentine between 2.5 and 50 μm. Icarus. **64**, 493–502 (1985). https://doi.org/10.1016/0019-1035(85)90070-3

Mu, F.F., Luiz, E.W., Fiedler, S.: On the dynamics and air-quality impact of the exceptional East Asian dust outbreak in mid-March 2021. Atmospheric Research **292**, 106846 (2023). https://doi.org/10.1016/j.atmosres.2023.106846

Mutschke, H., Begemann, B., Dorschner, J., Gurtler, J., Gustafson, B., Henning, T., Stognienko, R.: Steps toward interstellar silicate mineralogy - III. The role of aluminium in circumstellar amorphous silicates. Astron. Astrophys. **333**, 188–198 (1998)

Nousiainen, T.: Optical modeling of mineral dust particles: A review. Journal of Quantitative Spectroscopy and Radiative Transfer **110**, 1261–1279 (2009). https://doi.org/10.1016/j.jqsrt.2009.03.002

Ogawa, K., Schmugge, T., Rokugawa, S.: Estimating broadband emissivity of arid regions and its seasonal variations using thermal infrared remote sensing. IEEE Transactions on Geoscience and Remote Sensing **46**, 334–343 (2008). https://doi.org/10.1109/Tgrs.2007.913213

Park, S.S., Kim, J., Lee, J., Lee, S., Kim, J.S., Chang, L.S., Ou, S.: Combined dust detection algorithm by using MODIS infrared channels over East Asia. Remote Sens. Environ. **141**, 24–39 (2014). https://doi.org/10.1016/j.rse.2013.09.019

Peyridieu, S., Chédin, A., Capelle, V., Tsamalis, C., Pierangelo, C., Armante, R., Crevoisier, C., Crépeau, L., Siméon, M., Ducos, F., Scott, N.A.: Characterisation of dust aerosols in the infrared from IASI and comparison with PARASOL, MODIS, MISR, CALIOP, and AERONET observations. Atmos. Chem. Phys. **13**, 6065–6082 (2013). https://doi.org/10.5194/acp-13-6065-2013

Pierangelo, C., Chédin, A., Heilliette, S., Jacquinet-Husson, N., Armante, R.: Dust altitude and infrared optical depth from AIRS. Atmos. Chem. Phys. **4**, 1813–1822 (2004). https://doi.org/10.5194/acp-4-1813-2004

Posch, T., Baier, A., Mutschke, H., Henning, T.: Carbonates in space: The challenge of low-temperature data. Astrophys. J. **668**, 993–1000 (2007). https://doi.org/10.1086/521390

Prospero, J.M., Ginoux, P., Torres, O., Nicholson, S.E., Gill, T.E.: Environmental characterization of global sources of atmospheric soil dust identified with the Nimbus 7 Total Ozone Mapping Spectrometer (TOMS) absorbing aerosol product. Rev. Geophys. **40**, 2-1-2-31 (2002). https://doi.org/10.1029/2000rg000095

Roush, T.L., Esposito, F., Rossman, G.R., Colangeli, L.: Estimated optical constants of gypsum in the regions of weak absorptions: Application of scattering theories and comparisons to independent measurements. Journal of Geophysical Research: Planets (2007). https://doi.org/10.1029/2007je002920

Ryder, C.L., Marenco, F., Brooke, J.K., Estelles, V., Cotton, R., Formenti, P., McQuaid, J.B., Price, H.C., Liu, D.T., Ausset, P., Rosenberg, P.D., Taylor, J.W., Choularton, T., Bower, K., Coe, H., Gallagher, M., Crosier, J., Lloyd, G., Highwood, E.J., Murray, B.J.: Coarse-mode mineral dust size distributions, composition and optical properties from AER-D aircraft measurements over the tropical Eastern Atlantic. Atmos. Chem. Phys. **18**, 17225–17257 (2018). https://doi.org/10.5194/acp-18-17225-2018

Schuster, G.L., Dubovik, O., Holben, B.N.: Angstrom exponent and bimodal aerosol size distributions. Journal of Geophysical Research: Atmospheres (2006). https://doi.org/10.1029/2005jd006328

Scott, N.A., Chedin, A.: A fast Line-by-Line method for atmospheric absorption Computations - the automatized atmospheric absorption atlas. Journal of Applied Meteorology **20**, 802–812 (1981)

Segal-Rosenheimer, M., Linker, R.: Impact of the non-measured infrared spectral range of the imaginary refractive index on the derivation of the real refractive index using the Kramers-Kronig transform. Journal of Quantitative Spectroscopy and Radiative Transfer **110**, 1147–1161 (2009). https://doi.org/10.1016/j.jqsrt.2009.03.017

Serno, S., Winckler, G., Anderson, R.F., Hayes, C.T., McGee, D., Machalett, B., Ren, H.J., Straub, S.M., Gersonde, R., Haug, G.H.: Eolian dust input to the Subarctic North Pacific. Earth Planet. Sci. Lett. **387**, 252–263 (2014). https://doi.org/10.1016/j.epsl.2013.11.008

Shi, Z.B., Shao, L.T., Jones, T.P., Lu, S.L.: Microscopy and mineralogy of airborne particles collected during severe dust storm episodes in beijing, China. Journal of Geophysical Research: Atmospheres (2005). https://doi.org/10.1029/2004jd005073

Shin, J., Shin, D., Muller, D., Noh, Y.: Long-term analysis of AOD separated by aerosol type in East Asia. Atmos. Environ. **310**, 119957 (2023). https://doi.org/10.1016/j.atmosenv.2023.119957

Sobanska, S., Hwang, H., Choël, M., Jung, H.J., Eom, H.J., Kim, H., Barbillat, J., Ro, C.U.: Investigation of the chemical mixing state of individual Asian dust particles by the combined use of electron probe X-ray microanalysis and Raman microspectrometry. Anal. Chem. **84**, 3145–3154 (2012). https://doi.org/10.1021/ac2029584

Sokolik, I.N., Toon, O.B.: Incorporation of mineralogical composition into models of the radiative properties of mineral aerosol from UV to IR wavelengths. Journal of Geophysical Research: Atmospheres **104**, 9423–9444 (1999). https://doi.org/10.1029/1998jd200048

Sokolik, I.N., Toon, O.B., Bergstrom, R.W.: Modeling the radiative characteristics of airborne mineral aerosols at infrared wavelengths. Journal of Geophysical Research: Atmospheres **103**, 8813–8826 (1998). https://doi.org/10.1029/98jd00049

Soleimani, Z., Goudarzi, G., Sorooshian, A., Marzouni, M.B., Maleki, H.: Impact of middle Eastern dust storms on indoor and outdoor composition of bioaerosol. Atmos. Environ. **138**, 135–143 (2016). https://doi.org/10.1016/j.atmosenv.2016.05.023

Sorensen, C.M., Maughan, J.B., Moosmüller, H.: Spherical particle absorption over a broad range of imaginary refractive index. J. Quant. Spectrosc. Radiat. Transf. **226**, 81–86 (2019). https://doi.org/10.1016/j.jqsrt.2019.01.011

Stamnes, K., Tsay, S.C., Wiscombe, W., Jayaweera, K.: Numerically stable algorithm for Discrete-Ordinate-Method Radiative-Transfer in Multiple-Scattering and emitting layered media. Appl. Opt. **27**, 2502–2509 (1988). https://doi.org/10.1364/Ao.27.002502

Takenaka, H., Sakashita, T., Higuchi, A., Nakajima, T.: Geolocation correction for geostationary satellite observations by a Phase-Only correlation method using a visible channel. Remote Sensing **12**, 2472 (2020). https://doi.org/10.3390/rs12152472

Tegen, I., Lacis, A.A.: Modeling of particle size distribution and its influence on the radiative properties of mineral dust aerosol. Journal of Geophysical Research: Atmospheres **101**, 19237–19244 (1996). https://doi.org/10.1029/95JD03610

Thomas, M.E.: Infrared and Millimeter-Wavelength absorption by atmospheric Water-Vapor. Johns. Hopkins APL Tech. Dig. **8**, 363–369 (1987)

Volz, F.E.: Infrared Refractive-Index of atmospheric aerosol substances. Appl. Opt. **11**, 755–759 (1972). https://doi.org/10.1364/Ao.11.000755

Volz, F.E.: Infrared Optical-Constants of ammonium sulfate, Sahara dust, volcanic pumice, and flyash. Appl. Opt. **12**, 564–568 (1973). https://doi.org/10.1364/Ao.12.000564

Wan, S.M., Sun, Y.B., Nagashima, K.: Asian dust from land to sea: Processes, history and effect from modern observation to geological records. Geol. Mag. **157**, 701–706 (2020). https://doi.org/10.1017/S0016756820000333

Wang, X., Wen, H., Shi, J.S., Bi, J.R., Huang, Z.W., Zhang, B.D., Zhou, T., Fu, K.Q., Chen, Q.L., Xin, J.Y.: Optical and microphysical properties of natural mineral dust and anthropogenic soil dust near dust source regions over Northwestern China. Atmos. Chem. Phys. **18**, 2119–2138 (2018). https://doi.org/10.5194/acp-18-2119-2018

Wang, Y., Chen, L.F., Xin, J.Y., Wang, X.H.: Impact of the dust aerosol model on the VIIRS aerosol optical depth (AOD) product across China. Remote Sens. (Basel). **12**, 991 (2020). https://doi.org/10.3390/rs12060991

Wang, W.H., Shao, L.Y., Zhang, D.Z., Li, Y.W., Li, W.J., Liu, P.J., Xing, J.P.: Mineralogical similarities and differences of dust storm particles at Beijing from deserts in the North and Northwest. Sci. Total Environ. **803**, 149980 (2022). https://doi.org/10.1016/j.scitotenv.2021.149980

Wei, X.L., Chang, N.B., Bai, K.X., Gao, W.: Satellite remote sensing of aerosol optical depth: Advances, challenges, and perspectives. Crit. Rev. Environ. Sci. Technol. **50**, 1640–1725 (2020). https://doi.org/10.1080/10643389.2019.1665944

Wu, C.L., Lin, Z.H., Shao, Y.P., Liu, X.H., Li, Y.: Drivers of recent decline in dust activity over East Asia. Nat. Commun. **13**, 7105 (2022). https://doi.org/10.1038/s41467-022-34823-3

Xia, X.L., Min, J.Z., Wang, Y.B., Shen, F.F., Yang, C., Sun, Z.D.: Assimilating Himawari-8 AHI aerosol observations with a rapid-update data assimilation system. Atmos. Environ. **215**, 116866 (2019). https://doi.org/10.1016/j.atmosenv.2019.116866

Yu, H.B., Yang, Y., Wang, H.L., Tan, Q., Chin, M., Levy, R.C., Remer, L.A., Smith, S.J., Yuan, T.L., Shi, Y.X.: Interannual variability and trends of combustion aerosol and dust in major continental

outflows revealed by MODIS retrievals and CAM5 simulations during 2003–2017. Atmos. Chem. Phys. **20**, 139–161 (2020). https://doi.org/10.5194/acp-20-139-2020

Yu, T., Xiaole, P., Yujie, J., Yuting, Z., Weijie, Y., Hang, L., Shandong, L., Zifa, W.: East Asia dust storms in spring 2021: Transport mechanisms and impacts on China. Atmospheric Research **290**, 106773 (2023). https://doi.org/10.1016/j.atmosres.2023.106773

Zdanowicz, C., Hall, G., Vaive, J., Amelin, Y., Percival, J., Girard, I., Biscaye, P., Bory, A.: Asian dustfall in the st. Elias mountains, yukon, canada. Geochim. Cosmochim. Acta **70**, 3493–3507 (2006). https://doi.org/10.1016/j.gca.2006.05.005

Zeng, J., Xu, X.G., Wang, J., Wang, Y., Chen, X., Lu, Z.D., Torres, O., Reid, J.S., Miller, S.D.: Detecting layer height of smoke and dust aerosols over vegetated land and water surfaces via oxygen absorption bands. IEEE Int. Geosci. Remote Sens. Symp. Proc. pp 5588–5591 (2020). https://doi.org/10.1109/Igarss39084.2020.9323130

Zhang, C., He, J.Y., Yao, X.H., Mu, Y.C., Guo, X.Y., Ding, X.K., Yu, Y., Shi, J.H., Gao, H.W.: Dynamics of phytoplankton and nutrient uptake following dust additions in the Northwest Pacific. Sci. Total Environ. **739**, 139999 (2020). https://doi.org/10.1016/j.scitotenv.2020.139999

Zhang, Y.H., Saito, M., Yang, P., Schuster, G., Trepte, C.: Sensitivities of spectral optical properties of dust aerosols to their mineralogical and microphysical properties. Journal of Geophysical Research: Atmospheres **129**, e2023JD040181 (2024a). https://doi.org/10.1029/2023JD040181

Zhang, Z.S., Kuang, Z.Q., Yu, C.X., Wu, D.C., Shi, Q.B., Zhang, S., Wang, Z.Z., Liu, D.: Trans-Boundary dust transport of dust storms in Northern china: A study utilizing Ground-Based lidar network and CALIPSO satellite. Remote Sens. (Basel) **16**, 1196 (2024b). https://doi.org/10.3390/rs16071196

Zheng, J.Y., Zhang, Z.B., Garnier, A., Yu, H.B., Song, Q.Q., Wang, C.X., Dubuisson, P., Di Biagio, C.: The thermal infrared optical depth of mineral dust retrieved from integrated CALIOP and IIR observations. Remote Sens. Environ. **270**, 112841 (2022). https://doi.org/10.1016/j.rse.2021.112841

Zheng, J.Y., Zhang, Z.B., Yu, H.B., Garnier, A., Song, Q.Q., Wang, C.X., Di Biagio, C., Kok, J.F., Derimian, Y., Ryder, C.: Thermal infrared dust optical depth and coarse-mode effective diameter over oceans retrieved from collocated MODIS and CALIOP observations. Atmos. Chem. Phys. **23**, 8271–8304 (2023). https://doi.org/10.5194/acp-23-8271-2023